

Free Discontinuity Regression

With an Application to the Economic Effects of Internet Shutdowns

Florian Gunsilius¹ and David Van Dijcke^{2,3}

¹Department of Economics, Emory University

²Department of Economics, University of Michigan

³Risk Analytics Division, Ipsos Public Affairs

May 9, 2025

Abstract

Sharp, multidimensional changepoints—abrupt shifts in a regression surface whose locations and magnitudes are unknown—arise in settings as varied as gene-expression profiling, financial covariance breaks, climate-regime detection, and urban socioeconomic mapping. Despite their prevalence, there are no current approaches that jointly estimate the location and size of the discontinuity set in a one-shot approach with statistical guarantees. We therefore introduce Free Discontinuity Regression (FDR), a fully nonparametric estimator that simultaneously (i) smooths a regression surface, (ii) segments it into contiguous regions, and (iii) provably recovers the precise locations and sizes of its jumps. By extending a convex relaxation of the Mumford–Shah functional to random spatial sampling and correlated noise, FDR overcomes the fixed-grid and i.i.d. noise assumptions of classical image-segmentation approaches, thus enabling its application to real-world data of any dimension. This yields the first identification and uniform consistency results for multivariate jump surfaces: under mild SBV regularity, the estimated function, its discontinuity set, and all jump sizes converge to their true population counterparts. Hyperparameters are selected automatically from the data using Stein’s Unbiased Risk Estimate, and large-scale simulations up to three dimensions validate the theoretical results and demonstrate good finite-sample performance. Applying FDR to an internet shutdown in India reveals a 25–35% reduction in economic activity around the estimated shutdown boundaries—much larger than previous estimates. By unifying smoothing, segmentation, and effect-size recovery in a general statistical setting, FDR turns free-discontinuity ideas into a practical tool with formal guarantees for modern multivariate data.

Keywords: bounded variation, internet shutdowns, Mumford–Shah functional, non-parametric regression, segmentation, discontinuity.

fgunsil@emory.edu, dvdiijcke@umich.edu. Authors listed alphabetically. Python code for this paper can be found at <https://github.com/Davidvandijcke/fdr> We thank Austin Wright as well as audiences at the Bank of England, Emory, MIT, Northwestern, Princeton, Simon Fraser, UIUC, the University of Michigan, Yale, the 2023 Munich Econometrics conference, the 2023 European Winter Meetings of the Econometric Society, and the 2024 ESIF Economics and AI+ML Meeting for helpful comments and suggestions. All errors are our own.

1 Introduction

In many settings of interest, discontinuous changes in regression surfaces can reveal fundamental insights into the underlying problem structure, with both location and size of discontinuities typically unknown and dependent on multiple variables. Such discontinuities arise in many contexts, including algorithmic decision-making in finance and education, marketing segmentation, and tipping points in climate, urban sorting, financial markets, and spatial gene-expression profiling (Argyle et al., 2020; Brunner et al., 2021; Kuo et al., 2002; Li et al., 2010; Lamberson and Page, 2012; Card et al., 2008; Scheffer et al., 2009; Hansen, 2017; Caetano and Maheshri, 2017; Aue et al., 2009; Chen et al., 2023; Hou et al., 2023).

We introduce *Free Discontinuity Regression* (FDR), a method that reconstructs the regression surface *and* the exact geometry and magnitude of its jumps in one shot. FDR segments the domain into smooth and discontinuous regions without any point-wise smoothness assumption. In contrast to wavelet smoothing, fused-lasso variants, or gradient-threshold rules, our approach embeds smoothing and boundary detection in the same optimization, so the jump set and its sizes emerge as primary estimands rather than as results of a second-stage thresholding procedure, allowing us to develop the first formal identification guarantees for both jump location and size estimation in any dimension.

Our starting point is the Mumford-Shah (MS) functional (Mumford and Shah, 1989), a workhorse model from mathematical computer vision and extension of classic discrete approaches (Geman and Geman, 1984), which jointly segments and denoises while incorporating spatial regularity. The MS functional arises naturally as a solution to the limitations of simpler edge detection and thresholding methods (Canny, 1986; Kass et al., 1988), which almost surely misclassify discontinuities in noisy settings (Chan and Shen, 2005) and typically require multiple estimation steps, complicating statistical inference.¹ The MS functional is non-convex, so its critical points need not be global optima. This poses a threat to the reproducibility of estimates and the ability to characterize convergence to the true population function. To resolve it, we employ the method of calibrations (Alberti et al., 2003) to obtain a convex relaxation with global solutions, implementable via primal-dual algorithms (Chambolle and Pock, 2011).

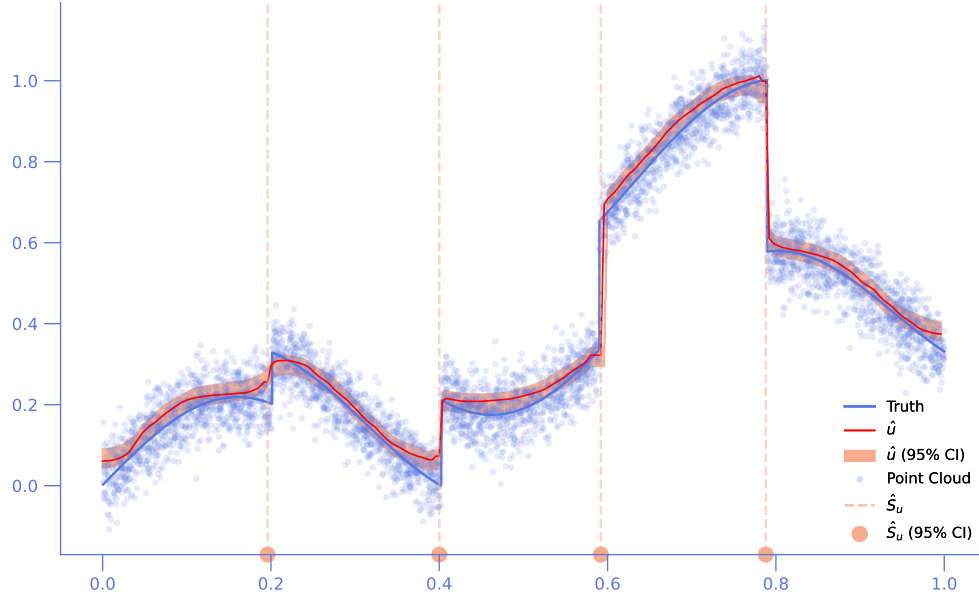
Most classical approaches to the MS functional treat the noise as already baked into *fixed* image f . Although f may deviate from the true underlying signal u , the analysis typically does not place a probability distribution over all possible noisy images; rather, f is taken as a single, deterministic function. In contrast, our statistical viewpoint treats the observed

¹For empirical validation of the MS functional’s superiority over simpler approaches, see Wang et al. (2012); Chan and Vese (2001); Lucas et al. (2022); Strekalovskiy et al. (2012).

function Y_i as doubly random: the function values are observed with random noise, and live in a random point cloud. Caroccia et al. (2020) recently considered a similar setting for the Mumford-Shah functional on random graphs generated by random point clouds, where the noise is additive and i.i.d. In contrast, we work with a random grid on a random point cloud, and allow for the noise to be correlated. This is important in spatial settings like our application, and even in the classical image setting, where we can expect noise in blurry segments of the image to be correlated. Moreover, we provide sharp identification results in any dimension, in addition to Γ -convergence—the first results of their kind, to our knowledge. These complement and extend recent results for discrete approximations of the classical non-convex MS functional (Caroccia et al., 2020; Ruf, 2019; Morini, 2002; Richardson, 1992) and related functionals (Chambolle and Pock, 2021; García Trillos and Slepčev, 2016; García Trillos and Murray, 2017; Hütter and Rigollet, 2016; Hu et al., 2022).

Figure 1 demonstrates our method on 1D-3D simulated examples, showing accurate recovery of both functions and discontinuities from noisy data. We note that, while our main contribution lies in estimating multivariate discontinuities, our method also performs remarkably well in the one-dimensional case, handling multiple jumps of different sizes effortlessly without requiring user input on the number of jumps or the minimum jump size. Further below, we apply the method to estimate the effects of an internet shutdown in Rajasthan, India, in 2021. This one-day shutdown, implemented to prevent exam cheating, created sharp geographic discontinuities in connectivity. Using anonymized mobile activity around economic points of interest and cached location data from satellite-connected apps, we estimate a 25-35% reduction in economic activity along the shutdown boundary. These findings substantially exceed previous estimates and highlight the asymmetry between internet expansion and shutdowns in modern economies, as well as the critical importance of reliable digital infrastructure for economic performance.

Our method advances several literatures. For a concise overview of how it compares to the main competing methods, see Table 1. The rich literature on change point detection methods typically focuses on discontinuity locations rather than magnitudes, or on the one-dimensional setting (Page, 1954; Müller, 1992; Braun et al., 2000; Killick et al., 2012; Porter and Yu, 2015; Donoho and Johnstone, 1994; Harchaoui et al., 2008), while structural break estimation primarily addresses time series (Andrews, 1993; Bai and Perron, 2003; Delgado and Hidalgo, 2000). Recent extensions to multivariate domains either impose structural assumptions (Park, 2022; Herlands et al., 2019; Zhu et al., 2014), omit regression estimation (Madrid Padilla et al., 2022), require treatment status to be observed (Herlands et al., 2018), or assume known discontinuity locations (Cheng, 2023; Narita and Yata, 2021; Abdulkadiroğlu et al., 2022; Cattaneo and Titiunik, 2022; Keele and Titiunik, 2015). Classical



(a) 1D: Truth + Point Cloud + \hat{u} + Boundary

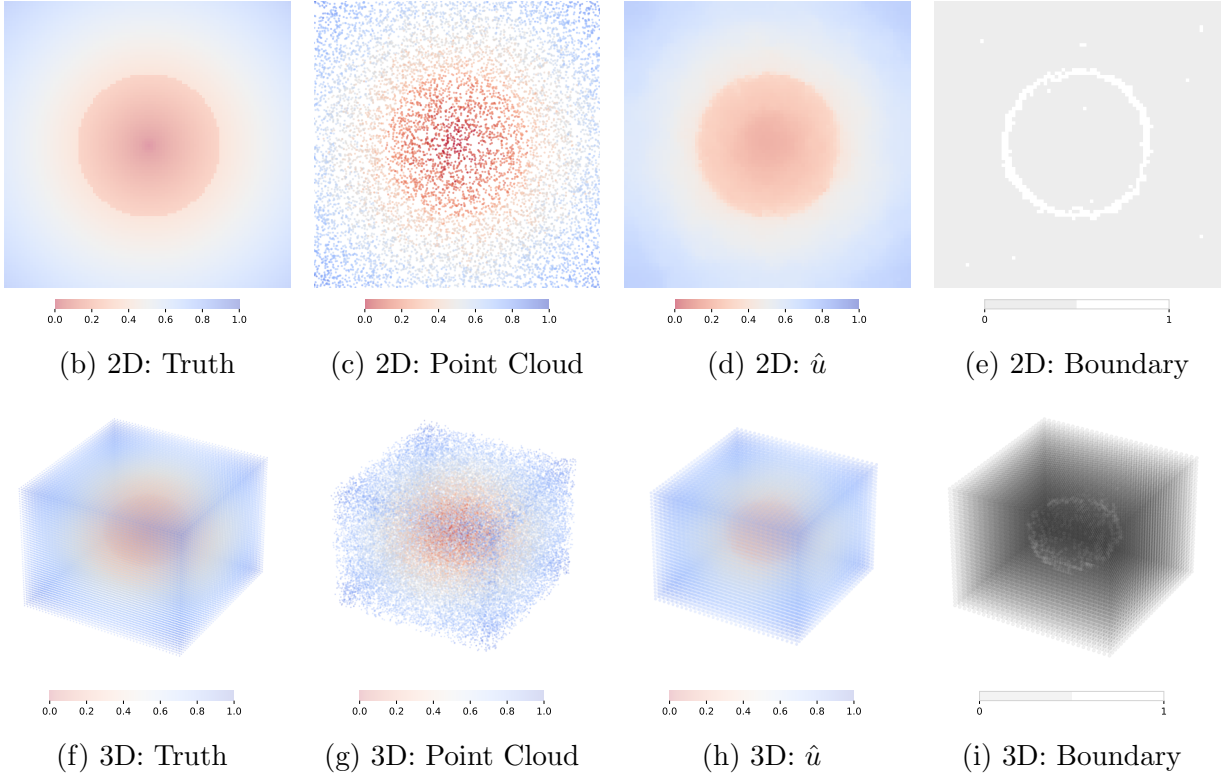


Figure 1: Simulations: 1D to 3D

Notes: figures depict, for 1D–3D; the true underlying function without noise, the random point cloud with Gaussian noise ($\sigma = 0.05$), the estimated response function \hat{u} and the estimated boundary locations. 1D case also includes red shaded 95% confidence bands estimated by subsampling with an estimated rate of convergence (Politis et al., 1999), and red dots below the plot to indicate jump sizes that are different from 0 at 95% level. Hyperparameters for 1D, 2D chosen by SURE. *Details:* **1D** jump sizes: 0.1286, 0.2133, 0.3192, -0.4220 ($d = 0.2823, 0.4682, 0.7005, -0.9262$), $n=5,000$, $\lambda = 98.6712, \nu = 0.0001$. **2D** jump size $\alpha = 0.1126$ ($d = 0.75$), $n=10,000$; $\lambda = 48.3921, \nu = 0.0012$; **3D** jump size $\alpha = 0.0738$ ($d = 0.5$), $n=50,000$; $\lambda = 10, \nu = 0.008$.

multivariate jump regression approaches (Qiu and Yandell, 1997; Korostelev and Tsybakov, 1993; O’Sullivan and Qian, 1994; Muller and Song, 1994; Donoho, 1999; Li and Ghosal, 2017; Qiu, 1998) often require knowing partition counts or limit dimensionality. The fused lasso literature (Tibshirani et al., 2005; Rinaldo, 2009; Harchaoui and Lévy-Leduc, 2010) has mostly focused on piecewise constant approximations. Recent approaches have made progress on estimating multivariate, piecewise-smooth regression surfaces with discontinuities, but do not develop any formal approaches for estimating the jump sizes and locations, instead relying on post-estimation thresholding without formal guarantees (Park, 2022; Caroccia et al., 2020; Zhu et al., 2014). Finally, note that there is also a rich but distinct literature on “multiple changepoints” that deals with the setting where the *outcome variable* is multivariate or functional (Aue et al., 2009; Matteson and James, 2014; Fryzlewicz, 2014; Kovács et al., 2023; Madrid Padilla et al., 2022; Dubey and Müller, 2020; Horváth et al., 2021), as opposed to our setting where the *regressors* are. A notable contribution in that literature is Madrid Padilla et al. (2023) who allow the multivariate output signals to be correlated and only satisfy mixing conditions, in line with our setting for a univariate output with multivariate domain.

Our approach, on the contrary, explicitly estimates the piecewise-smooth regression function jointly with its jump locations and sizes. Moreover, we provide formal convergence and identification results for both, which to our knowledge are the first of their kind for the general multivariate setting. Additionally, all existing multivariate estimation approaches assume that the sampling noise is i.i.d. across data points or pixels, while we allow it to be correlated under a general mixing process. This is crucial for frequently occurring spatiotemporally dispersed jump processes like climate regimes, geographic policy discontinuities, or financial time series. Finally, unlike many existing methods, which often work on a fixed lattice, we allow for randomness in both the locations and the sampling error of the data points.

2 Free Discontinuity Regression

In this section, we develop the statistical framework for estimating regression functions with unknown discontinuities of any dimension. All mathematical notation is detailed in Appendix A.

Table 1: Comparison of Statistical Methods for Multivariate Jump Surface Estimation

Method	Jump Domain	Jump Location	Jump Size	Jump Identification	Correlated Sampling/Noise
Proposed Method ¹	Any D	✓	✓	✓	✓
Wild Binary Segmentation ²	1D	✓	×	✓	×
PELT ³	1D	✓	×	×	✓
TV Denoising/Fused Lasso ⁴	Any D	~ ^a	~ ^a	×	×
Trend Filtering on Graphs ⁵	Graph	~ ^a	~ ^a	×	×
Change Surfaces ⁶	Any D	~ ^b	~ ^b	×	× ^b
Jump Gaussian Processes ⁷	Any D	~ ^c	~ ^c	×	×
SVCM ⁸	Any D	~ ^a	~ ^a	×	~ ^d
MS on Graphs ⁹	Graph	~ ^e	~ ^e	×	×

Legend. × = No; ✓ = Yes; ~ = Partially or requires additional assumptions/extensions.

Jump Domain denotes the dimension of the Euclidean point cloud on which the function is observed (or “Graph” if defined on a network); **Jump Location/Size** records whether those quantities are explicitly estimated; **Jump Identification** flags formal convergence results; **Correlated Sampling/Noise** indicates support for correlated noise in the model.

^a Requires post-estimation gradient thresholding; no explicit discussion of discontinuity identification.

^b Models smooth transition boundaries with Gaussian processes; no explicit discussion of discontinuity identification.

^c Estimates local (not global) piecewise-continuous regressions.

^d Errors are i.i.d. samples from a stochastic process; input locations are i.i.d.

^e Jump recovery done via manual gradient thresholding.

¹Gunsilius and Van Dijke (2025) ²Fryzlewicz (2014) ³Killick et al. (2012) ⁴General version in Hütter and Rigollet (2016)

⁵Wang et al. (2016) ⁶Herlands et al. (2019) ⁷Park (2022) ⁸Zhu et al. (2014) ⁹Caroccia et al. (2020).

2.1 Regression framework

We consider n randomly sampled units indexed by $i = 1, 2, \dots, n$ for which we observe a potentially multivariate regressor $X_i \in \mathbb{R}^d$ and an outcome of interest $Y_i \in \mathbb{R}$. The regression model is

$$(1) \quad Y_i = f(X_i) + \varepsilon_i, \quad \mathbb{E}[\varepsilon_i | X_i] = 0,$$

where the ε_i are unobservable error terms. Our goal is to estimate both the regression surface $f(x)$ and its discontinuity set S_f . To handle multivariate regressors, we need to extend the notion of a univariate discontinuity to multiple dimensions. Following Definition 2 in Appendix A (Ambrosio et al., 2000, Definition 3.67), we characterize jump points of a function u on \mathcal{X} through two distinct limiting values, $u^+(x)$ and $u^-(x)$, called *traces*. These traces reflect how u behaves as one approaches a point x in the domain from opposite sides, with an orientation vector ρ defining these “sides.” The collection of all such jump points forms the (*approximate*) *discontinuity set* S_u .

2.2 FDR as an estimator based on the Mumford-Shah Functional

Standard approaches to this estimation problem face several fundamental limitations. Smoothing methods do not explicitly estimate discontinuity locations or sizes, but merely approximate the regression surface while preserving discontinuities. This leads to downward-biased jump size estimates in practice (see e.g. [Caroccia et al., 2020](#), Fig. 7.1f). Simple thresholding approaches that estimate jump locations via gradient steepness almost surely misclassify discontinuities in noisy settings and fail to take into account the spatial regularity of the function that produces the jumps, resulting in severely biased estimates and high false positive and negative rates for jump detection ([Chan and Shen, 2005](#)). The Mumford-Shah (MS) functional ([Mumford and Shah, 1989](#)) addresses these issues by combining smoothing and thresholding in a unified framework.

2.2.1 The Mumford-Shah Functional

Assuming the random variable X has density f_X , our statistical version of the MS functional takes the form:

$$(2) \quad E(u) = \underbrace{\lambda \int_{\mathcal{X}} (f(x) - u(x))^2 f_X(x) dx}_{\text{Regression}} + \underbrace{\int_{\mathcal{X} \setminus S_u} |\nabla u(x)|^2 f_X(x) dx}_{\substack{\text{Roughness penalty} \\ \text{away from discontinuity}}} + \underbrace{\nu \mathcal{H}^{d-1}(S_u)}_{\substack{\text{Discontinuity regularity} \\ \text{penalty}}}.$$

The functional combines three components: 1) A regression term that minimizes the mean-squared error between the true function f and its approximation u ; 2) a roughness penalty that controls the gradient size of u away from the discontinuity set S_u ; 3) a penalty on the “size” of the discontinuity set, measured by its $(d-1)$ -dimensional Hausdorff measure \mathcal{H}^{d-1} . The goal is to estimate the minimizer u of this function, which immediately delivers an estimate of the discontinuity set S_u as well as the jump sizes $u^+(x) - u^-(x)$ for each jump point $x \in S_u$.

The hyperparameters $\lambda, \nu \geq 0$ control the balance between function smoothness and boundary complexity, with the gradient term’s weight normalized to 1. The squared Euclidean norm in \mathbb{R}^d is denoted by $|\cdot|^2$.

2.2.2 Convexification Through Calibrations

The MS functional’s non-convexity through its third term threatens consistent estimation, as optimization routines need not converge to global optima. In practice, this manifests as spurious discontinuities and boundaries ([Brown et al., 2012](#), Fig. 4-5; [Pock et al., 2009](#), Fig. 5).

A common approach to non-convex optimization is to re-estimate the model multiple times with different initializations and select the solution that minimizes the objective function. However, this approach becomes computationally infeasible for functional minimands with dimension larger than 1, as the set of potential initializations grows too large. Moreover, it is not guaranteed to converge to the true global minimum. We resolve this using calibrations (Alberti et al., 2003; Pock et al., 2010), which lift the problem to a higher dimension by considering the graph Γ_f of f . The key is finding a vector field $p : \mathbb{R}^{d+1} \rightarrow \mathbb{R}^{d+1}$ on the lifted space that maximizes flux through the graph. This yields the convex relaxation:

$$E(u) = \sup_{p \in K} \int_{\mathcal{X} \times \mathbb{R}} p \cdot D\mathbb{1}_u$$

with a convex constraint set

$$K = \left\{ p \in C_0(\mathcal{X} \times \mathbb{R}, \mathbb{R}^{d+1}) : \right. \\ \left. p^t(x, t) \geq \frac{|p^x(x, t)|^2}{4f_X(x)} - \lambda f_X(x)(t - f(x))^2, \quad \left| \int_{t_1}^{t_2} p^x(x, s) ds \right| \leq \nu, \quad \forall t_1, t_2 \in \mathbb{R} \right\}.$$

Here, t indexes the lifted dimension, and $\mathbb{1}_u(x, t)$ is the indicator function of the subgraph of $u(x)$, taking value 1 if $t < u(x)$ and 0 otherwise. The measure $D\mathbb{1}_u := (D_1\mathbb{1}_u, \dots, D_{d+1}\mathbb{1}_u)$ is $(d+1)$ -dimensional Radon measure, with p^x and p^t denoting the first d and last components of $p \in C_0(\mathcal{X} \times \mathbb{R}, \mathbb{R}^{d+1})$ respectively. To also achieve convexity over the target function space, we follow Pock et al. (2009) and optimize over the more general space of functions mapping to the unit interval:

$$v(x, t) \in C := \left\{ v \in SBV(\mathcal{X} \times \mathbb{R}, [0, 1]) : \lim_{t \rightarrow -\infty} v(x, t) = 1, \lim_{t \rightarrow +\infty} v(x, t) = 0 \right\}.$$

Here, $SBV(\mathcal{X} \times \mathbb{R}, [0, 1])$ denotes the space of special functions of bounded variation mapping to the unit interval. This class is particularly well-suited to our problem as it naturally accommodates functions with discontinuities while still being small enough to be controllable.

Definition 1. *The Free Discontinuity Regression estimator is the 0.5-level set of the optimizer v^* of the optimization problem*

$$(3) \quad \inf_{v \in C} E(v) := \inf_{v \in C} \sup_{p \in K} \langle p, Dv \rangle \equiv \inf_{v \in C} \sup_{p \in K} \int_{\mathcal{X} \times \mathbb{R}} p \cdot Dv.$$

This optimization problem is well-behaved due to its convexity and admits a solution under mild conditions:

Proposition 1. *The optimization problem (3) admits a global solution v^* in $SBV(\mathcal{X} \times \mathbb{R}) \cap \{v : |Dv| \leq c\}$ for fixed $c < +\infty$ if $f \in SBV(\mathcal{X})$.*

While the solution v^* need not take the form of an indicator function—which is required for the relaxation to be tight—we prove that it converges to one as $\lambda \rightarrow +\infty$ in a certain topology (Theorem 1). In practice, our automatic hyperparameter selection procedure selects values of λ that are many orders of magnitudes larger than the selected ν , and as such also leads to estimated solutions that are indicator functions in practice. Following Pock et al. (2009), we obtain the underlying function u by thresholding v at the 0.5-level set. When v is an indicator function, any threshold $t \in (0, 1)$ would yield equivalent results; the midpoint is natural when the solution deviates slightly from an indicator.

3 Statistical Properties

This section establishes the mathematical and statistical properties of the estimator. We first show that the solution to (3) recovers both the true discontinuity set and jump sizes as $\lambda \rightarrow +\infty$ with fixed $\nu > 0$. We then prove consistency of our empirical estimator via Γ -convergence (Dal Maso, 2012). All proofs appear in Appendix C.

We also provide practical tools for implementation: a data-driven method for selecting tuning parameters λ, ν using Stein’s unbiased risk estimate (SURE), and two approaches to uncertainty quantification. The first uses subsampling with estimated convergence rates (Politis et al., 1999) and should be used for estimation procedures, while the second employs split conformal inference (Lei et al., 2018) for computationally efficient uncertainty quantification in high-dimensional prediction.

3.1 Identification of the Discontinuity Sets and Jump Sizes

We first establish that the true function f is identified under mild regularity conditions. Specifically, we show that for fixed $\nu > 0$ and as $\lambda \rightarrow +\infty$, the solution to (3) recovers both the correct discontinuity set and jump sizes. This complements and extends previous results (Richardson, 1992; Morini, 2002) which established convergence of the discontinuity set for the classical non-convex Mumford-Shah functional. This result is the first to provide mathematical and statistical properties for the convexified problem.

We require two assumptions, following Richardson (1992). Let S_f denote the discontinuity set of f , which includes the jump set J_f and coincides with it \mathcal{H}^{d-1} -almost everywhere by the Federer-Vol’pert theorem (Ambrosio et al., 2000, Theorem 3.78).

Assumption 1. The density f_X is bounded above and below everywhere on its support \mathcal{X} , i.e., $0 < c_x \leq f_X(x) \leq \frac{1}{c_x} < +\infty$ for all $x \in \mathcal{X}$. Further, $f \in SBV(\mathcal{X})$ and there is a constant $c > 0$ such that $|f(x)| \leq c$ for \mathcal{L}^d -almost every $x \in \mathcal{X}$. Moreover, $\int_{\mathcal{X}} |\nabla f|^2 dx + \mathcal{H}^{d-1}(S_f) < +\infty$.

Assumption 2. For any $x \in S_f$ it holds that $\mathcal{H}^{d-1}(S_f \cap B_\rho(x)) > 0$ for all $\rho > 0$. Moreover, for any set $A \subset \mathcal{X}$ with $\text{dist}(A, S_f) > 0$ there exists a constant $L > 0$ such that $|f(x) - f(y)| \leq L|x - y|$ for any $x, y \in A$.

Assumption 1 imposes standard boundedness on the functions and their jump sizes. Assumption 2 ensures regularity both at and away from the discontinuity set. The first part implies connectedness of the discontinuity set when measured with \mathcal{H}^{d-1} on \mathcal{X} (e.g., precluding isolated points in two dimensions). This ensures $\mathcal{H}^{d-1}((\mathcal{X} \cap \bar{S}_f) \setminus S_f) = 0$, meaning the closure \bar{S}_f coincides with S_f \mathcal{H}^{d-1} -almost everywhere (Ambrosio et al., 2000, p. 337).

Theorem 1. Let Assumptions 1 and 2 hold. Then for fixed $\nu > 0$ and in the limit as $\lambda \rightarrow +\infty$ every sequence of solutions $v^*(\lambda)$ to (3) satisfies $\lim_{\lambda \rightarrow +\infty} \nabla v^*(\lambda) = 0$ \mathcal{L}^{d+1} -almost everywhere. Moreover, the jump set $J_{v^*}(\lambda)$ converges in Hausdorff distance d_H to the graph Γ_f , i.e.

$$\lim_{\lambda \rightarrow +\infty} d_H(J_{v^*}(\lambda), \Gamma_f) = 0.$$

The proof of 1 requires λ to diverge “fast enough” based on the countable rectifiability (Mattila, 1999) of the jump set: for any given sequence $\{r_m\}$ converging to 0 defining the lower density (Ambrosio et al., 2000) of the jump set, we need $\{\lambda_m\}$ such that $\lambda_m r_m \rightarrow +\infty$. This is not a restriction since λ can be arbitrarily large. In practice, λ must substantially exceed ν to identify correct jump sizes. Our hyperparameter selection procedure consistently finds such values, with λ orders of magnitude larger than ν , yielding convergent estimates of both jump set and sizes as N grows. We now turn to the practical implementation and the corresponding estimator.

3.2 The Empirical Estimator and Convergence

We now develop the empirical version of the estimator for observed data. Consider a random sample $\{X_i, Y_i\}_{i=1}^n$ from distribution $P_{Y,X}$, with errors ε_i , which can be correlated and not identically distributed, as long as they satisfy a law of large numbers. This is important for the spatial setting in our application, where the error terms in the nonparametric regression are correlated in general. Sufficient for this are mixing conditions. In the following, to

guarantee consistency of the kernel density estimator $\hat{f}_{X,h(n)}$, we assume that the marginal data generating process $\{X_i\}_{i \in \mathbb{N}}$ is stationary. This can be relaxed (Irle, 1997).

The key challenges in moving to random data are twofold:

- (i) First, the random location of the points. Unlike computer vision applications (Pock et al., 2009) where values lie on a fixed lattice, our observations occur at arbitrary points in the domain. While recent approaches handle this using nearest-neighbor graphs (Caroccia et al., 2020; Chambolle et al., 2017; Chambolle and Pock, 2021), such methods are less suitable here as our constraint set K requires explicit dimension-wise operations, particularly summation over one dimension.
- (ii) The second source of randomness is the error term ε_i . In contrast to existing image segmentation approaches, we allow the terms ε_i to be dependent, that is, a strongly mixing process.

To accommodate the random locations, we discretize (3) on a regular grid following Pock et al. (2009). Specifically, we overlay an $(N_1 \times N_2 \times \dots \times N_d) \times S$ pixel grid on the random point cloud $\{X_i\}_{i=1}^n$, defining $\mathcal{Q}_N = \{(k_1, \dots, k_d, s) : k_i = 1, 2, \dots, N_i; \dots; k_d = 1, \dots, N_d; s = 1, 2, \dots, S\}$. To ease notation, we assume without loss of generality that all dimensions are discretized in the same manner, $s := k_{d+1}$, $N_1, \dots, N_{d+1} = N$. Also, denote $k := (k_1, \dots, k_{d+1})$, and $k_- := (k_1, \dots, k_d)$. The empirical analogue of $v \in C$ becomes

$$\hat{v}_{Nn}(x) \equiv \hat{v}_{Nn}(\tilde{x}, t) := \sum_{1 \leq k_1, \dots, k_{d+1} \leq N} v_{k_1, \dots, k_{d+1}} \mathbb{1} \{x \in Q_{k_1, \dots, k_{d+1}}\}$$

where v_k is assigned to the center of cube Q_k . We define the empirical analogue p_N of $p \in K$ to take values on the boundary of the respective cubes. That is, for each $j = 1, \dots, d+1$, the corresponding value $p_{k_1, \dots, k_j + \frac{1}{2}, \dots, k_{d+1}}$ lies on the boundary $\partial Q_{k_1, \dots, k_j, \dots, k_{d+1}} \cap \partial Q_{k_1, \dots, k_j + 1, \dots, k_{d+1}}$. This preserves duality in the empirical setting, as the empirical analogues of p are defined on boundaries of the cubes, while the analogues of v are defined in the center (Chambolle and Pock, 2021). Problem (3) becomes

$$(4) \quad \min_{v \in \tilde{C}_N} \hat{E}_{Nn}(v) := \min_{v \in \tilde{C}_N} \max_{p \in \tilde{K}_{Nn}} \langle p, D_N v \rangle_N$$

with

$$\begin{aligned}\tilde{C}_N &= \{v : v(k) \in [0, 1], v(k_1, \dots, k_d, 1) = 1, v(k_1, \dots, k_d, N) = 0\} \\ \hat{K}_{Nn} &= \left\{ p = (p^x, p^t)^T : p^t(k) \geq \frac{|p^x(k)|^2}{4 \hat{f}_{X,h(n)}(k_-)} - \lambda \hat{f}_{X,h(n)}(k_-) \left(\frac{k_{d+1}}{N} - \hat{f}_{Nn}(k_-) \right)^2, \right. \\ &\quad \left. \left| \frac{1}{N} \sum_{s_1 \leq k_{d+1} \leq s_2} p^x(k) \right| \leq \nu \right\},\end{aligned}$$

where $D_N v$ is the normalized forward difference and $\langle p, Dv \rangle_N$ the scalar product between two vectors,

$$\langle p_N, D_N v_N \rangle_N = \sum_{0 \leq k_1, \dots, k_{d+1} \leq N} N \left(v_{k_1, \dots, k_{d+1}}^\uparrow - v_{k_1, \dots, k_{d+1}} \right) p_{k_1, \dots, k_{d+1}},$$

with $v_{k_1, \dots, k_j, \dots, k_{d+1}}^\uparrow := v_{k_1, \dots, k_j+1, \dots, k_{d+1}}$ and $p_k^\uparrow = p_k \cdot e^\uparrow$. The constraints hold for all grid points k , and $s_1 \leq k_{d+1} \leq s_2$ iterates over indices with $1 \leq s_1 \leq k_{d+1} \leq s_2 \leq S$.

For function estimation, we use weighted averages within each grid cube:

$$\hat{f}_{Nn}(\bar{x}_{k_-}) = \sum_{i: X_i \in Q_{k_-}} w_i Y_i$$

where \bar{x}_{k_-} is the cube center and weights w_i sum to 1; for simplicity, we assume uniform weights, i.e., $w_i = 1/\#\{i : X_i \in Q_k\}$. We estimate the density f_x via a standard Nadaraya-Watson estimator

$$\hat{f}_{X,h(n)} = \frac{1}{nh(n)^d} \sum_{i=1}^n K\left(\frac{X_i - x}{h(n)}\right),$$

where $h(n)$ is a bandwidth and $K(\cdot)$ is a multivariate kernel. We assume that $K : \mathbb{R}^d \rightarrow \mathbb{R}$ satisfies $K(x\rho) \geq K(x)$ for all $x \in \mathbb{R}^d$ and $0 \leq \rho \leq 1$, $\int_{\mathbb{R}^d} K(x) dx = 1$, $K(x) = O(|x|^{-n-\rho})$ as $|x| \rightarrow +\infty$ for some $\rho > 0$, and that $\sup_{x \in \mathbb{R}^d} K(x) < +\infty$. In the following, we call such a kernel *regular* (Irle, 1997).

We make the following assumption on the data-generating process.

Assumption 3. *Let (Ω, \mathcal{A}, P) be a probability space and let the following hold:*

(i) *(Mixing assumption and sampling frequency)*

The number of grid cubes Q_k grows as $N^d(n) = O(n^m)$ for some $0 < m < 1$. Furthermore, $(Y_i, X_i, \varepsilon_i) : \Omega \rightarrow \mathbb{R} \times \mathbb{R}^d \times \mathbb{R}$ is an α -mixing sequence with $\alpha(u) = O(u^{-s})$ with $s > \max\left\{\frac{r+m}{1-m}, \frac{r+1}{2v+1(1-m)}\right\}$ for some $r > 1$ and $v \geq 3$. The marginal process $\{X_i\}_{i=1}^n$ is strictly stationary. The penalty term ν is fixed, and $\lambda_n = o(N(n))$.

(ii) *(Moment conditions)*

$\mathbb{E}[\varepsilon_i|X_i] = 0$ and the moment generating function $\mathbb{E}[\exp(t\varepsilon_i)]$ exists in a neighborhood of zero; also, $\mathbb{E}[|Y_i|^{r+\delta}] < M < +\infty$ for all i and some $\delta > 0$. The X_i have a common marginal density f_X , which has compact support \mathcal{X} and is bounded away from zero and infinity, i.e., $0 < c_x \leq f_X(x) \leq \frac{1}{c_x} < +\infty$ for all $x \in \mathcal{X}$.

(iii) *(Regularity of kernel and histogram estimator)*

Let $K : \mathbb{R}^d \rightarrow \mathbb{R}$ be a regular kernel and $h(n) \rightarrow 0$ with $nh(n)^d \rightarrow +\infty$ as $n \rightarrow +\infty$ and $\sum_{i=1}^{\infty} (i^2 h(i)^{d+d/l})^{-1} < +\infty$, where $0 < l < s$. The weights w_i in the histogram estimator take the form $w_i = 1 / \sum_{i=1}^n 1(X_i \in Q_k)$.

These regularity assumptions are standard. Part (i) requires a bound on the mixing parameter s that is very minor, since $r > 1$ can be as close to unity as we want. It involves the rate m at which the number N^d of grid points grows with the number of data points n . The slower this growth, the smaller the mixing constant can be. The strict stationarity assumption on $\{X_i\}_{i=1}^n$ is done for convenience in the proof and can be relaxed. Further, we allow the penalty term λ_n to vary with the data, but very slowly, in order to still obtain the almost sure convergence. The moment conditions in Part (ii) are very minor and allow for unbounded error terms ε_i as long as their tails decay quickly enough. The regularity for kernel and histogram estimators in Part (iii) are standard and taken from the kernel estimator results in [Irle \(1997\)](#).

Before proving the full statistical result, we provide a consistency result for the simpler setting where we pretend $f(x)$ is known and does not have to be estimated. This result is novel in the image recognition literature and complements recent convergence results in this area (e.g. [Chambolle and Pock, 2021](#)). It also showcases the complication when introducing the two sources of randomness.

Proposition 2. *Let Assumption 3 hold, let $\hat{f}_{N_n} \equiv f$ be a fixed function whose values are given in the center \bar{x}_k of each cube Q_k , and set $f_X(x) \equiv 1$ everywhere on \mathcal{X} . Then, for fixed penalty terms ν, λ , $E_N(v)$ Γ -converges in the weak*-topology to*

$$E(v) := \begin{cases} \sup_{p \in K} \int_{[0,1]^{d+1}} p \cdot Dv & \text{if } v \in C \\ +\infty & \text{else} \end{cases}.$$

Now we add the randomness to f as well as f_X . The fact that f has to be estimated through random draws complicates the estimation procedure significantly. In fact, any estimator \hat{f}_{N_n} for f that averages out the error caused by ε_i , including the proposed histogram estimator, converges to a precise representative \tilde{f} of f . This means that it is

consistent only for points $x \notin S_f$. For points $\tilde{x} \in S_f$, $\hat{f}_{N_n}(\tilde{x})$ converges almost surely to $\tilde{f}(\tilde{x}) = (1 - \theta)f^+(\tilde{x}) + \theta f^-(\tilde{x})$, that is, a convex combination of the values of the traces $f^+(\tilde{x})$ and $f^-(\tilde{x})$. The weight θ depends on the angle of the hyperplane induced by the approximate differential and the weighting from f_X . If all Q_k are cubes and f_X is the density of the uniform distribution, then $\theta = 1/2$. Importantly, $0 < \theta < 1$, which implies that the proposed estimator identifies the location of the jumps of f perfectly. This is captured in the following result.

Theorem 2. *Let Assumptions 1 – 3 hold. Then $\hat{E}_{N_n}(v)$ Γ -converges in the weak*-topology almost surely to*

$$\tilde{E}(v) := \begin{cases} \sup_{p \in \tilde{K}} \int_{\mathcal{X} \times \mathbb{R}} p \cdot Dv & \text{if } v \in C \\ +\infty & \text{else,} \end{cases}$$

where \tilde{K} is the same as the constraint K , but f replaced by

$$\tilde{f}(x) = \begin{cases} f(x) & \text{if } x \notin S_f \\ (1 - \theta)f^+(x) + \theta f^-(x) & \text{otherwise,} \end{cases}$$

where

$$\theta = \frac{\int_{Q_{kN} \cap H^+(x, \rho)} f(x) f_X(x) dx}{\int_{Q_{kN}} f_X(x) dx}$$

with $\{Q_{kN}\}_N$ the sequence of grid cubes containing and converging to $\{x\}$ and $H^+(x, \rho) = \{y : \langle y - x, \rho \rangle \geq 0\}$ a half space created by the hyperplane $H(x, \rho)$ at x oriented by $\rho \in S^{d-1}$ and separating the traces $f^+(x)$ and $f^-(x)$.

Complementing this with a compactness result yields convergence of the minimizer:

Corollary 1. *Let the assumptions from Theorem 2 hold and let \hat{v}_{N_n} be minimizers of $\hat{E}_{N,n}(v)$ with $v \in C \cap \{v \in SBV(\mathcal{X} \times \mathbb{R}) : |Dv| \leq 1\}$. Then $\hat{v}_{N_n} \rightarrow \tilde{v}$ in the weak*-topology almost surely, where \tilde{v} is a minimizer of the deterministic population objective $\tilde{E}(v)$.*

This shows that the estimator is consistent for a precise representative of f , identifying the correct jump locations as $\lambda_n \rightarrow +\infty$. As shown in the simulations in Figure 1, the proposed estimator also allows to identify the correct jump size, not just the location. The key for this is the weak*-convergence of the optimizer as proved in Theorem 2: by the closure of SBV (Ambrosio et al., 2000, Theorem 4.7), this implies that the traces of v_n converge \mathcal{H}^{d-1} -almost everywhere to the traces of v . Since the traces are identified, this also identifies the jump sizes directly. Finally, standard convergence results for level-sets (e.g. Camilli, 1999) imply

that the 0.5-level set, which is our estimator for the true function, also converges almost surely.

In practice, following the vision literature (Stekalovskiy and Cremers, 2014), we detect the empirical discontinuity set by thresholding the estimated gradient,

$$\hat{S}_u = \{x \in \mathcal{X} : \|\nabla \hat{u}_{N_n}(x)\| \geq \sqrt{\nu}\}.$$

That gives us the estimated jump locations. To estimate the corresponding jump sizes, for every boundary voxel $x \in \hat{S}_u$, we march in the estimated outward normal direction $\hat{\rho}_{N_n}(x)$ and in the inward direction $-\hat{\rho}_{N_n}(x)$ until we reach the first voxels $x_{N_n}^+(x)$ and $x_{N_n}^-(x)$ that lie *outside* the boundary mask \hat{S}_u . The empirical jump-size estimator is

$$\hat{\Delta}_{N_n}(x) = \hat{u}_{N_n}(x_{N_n}^+(x)) - \hat{u}_{N_n}(x_{N_n}^-(x)),$$

i.e. the difference between the “pure” function values immediately to the right and left of the interface. Because the march follows $\hat{\rho}_{N_n}(x)$, the construction automatically captures the correct orientation, so no grid refinement is needed. Then, Corollary 1 implies convergence of the empirical normal $\hat{\rho}_{N_n}(x)$ to the population normal to the jump set, and hence of the estimated jump sizes to their population counterparts.

Finally, we construct confidence bands using subsampling (Politis et al., 1999, Ch.8), which we choose over bootstrap methods due to the estimator’s non-smooth nature. The Online Appendix provides implementation details and describes a more computationally efficient alternative using conformal prediction.

3.3 Data-Driven Choice of Hyperparameters by SURE

While Theorem 1 establishes that the population estimator recovers the true jump locations and sizes as λ grows for fixed ν , optimal hyperparameter choice in finite samples depends on the data. We select λ, ν by minimizing Stein’s unbiased risk estimate (SURE) (Stein, 1981), which provides an asymptotically unbiased estimate of mean-squared error under Gaussian errors.

Given estimator $\hat{u}_\theta(Y)$ with hyperparameters $\theta = (\lambda, \nu)$, the Stein estimator is

$$(5) \quad \eta(\hat{u}_\theta(Y)) = \frac{1}{N} |Y - \hat{u}_\theta(Y)|^2 - \sigma^2 + 2\sigma^2 \operatorname{div}_Y \hat{u}_\theta(Y),$$

where $\operatorname{div}_Y \hat{u}_\theta(Y) := \sum_{i=1}^N \frac{\partial \hat{u}_{\theta,i}(Y_i)}{\partial Y_i}$ is the divergence with respect to the data. For continuous and bounded operators with well-defined divergence, $\eta(\hat{u}_\theta)$ is unbiased for $MSE(\hat{u}_\theta(Y)) :=$

$\frac{1}{N}|\hat{u}_\theta(Y) - f|^2$ (Ramani et al., 2008).

Since the estimator lacks a closed-form divergence, we use a Monte Carlo approximation by perturbing the data with random noise $\mathbf{b} \sim N(0, 1)$:

$$\text{div}_Y \hat{u}_\theta(Y) = \lim_{\delta \rightarrow 0} E_{\mathbf{b}} \left\{ \mathbf{b}' \left(\frac{\hat{u}_\theta(Y + \delta \mathbf{b}) - \hat{u}_\theta(Y)}{\delta} \right) \right\}.$$

Following Lucas et al. (2022), we average over R draws of $\mathbf{b}^{(r)}$ to obtain $\bar{\eta}^R(\hat{u}_\theta(Y)) := \frac{1}{R} \sum_{r=1}^R \eta_{\delta, \mathbf{b}^{(r)}}(\hat{u}_\theta(Y))$, setting $\delta = 0.01$. Monte Carlo simulations in the next section confirm that this approach selects effective hyperparameters.

3.4 Simulations

We validate the estimator on 1D, 2D, and 3D simulations with piecewise-smooth functions featuring jumps of varying magnitudes (Cohen’s $d = 0.25, 0.5, 0.75$). Additive Gaussian noise is set to $\sigma = 0.05$. We discretize the lifted dimension into 32 points (Pock et al., 2009) and select hyperparameters λ, ν via a Monte Carlo version of Stein’s unbiased risk estimate (MC-SURE) (Ramani et al., 2008; Lucas et al., 2022) on a 20×20 grid.

Figure 1 shows the true functions, noisy point clouds, and estimated surfaces for sample sizes of $n = 5,000$ (1D), $n = 10,000$ (2D), and $n = 50,000$ (3D). The method accurately recovers both location and magnitude of discontinuities. In the 1D case, we also plot 95% confidence bands computed via subsampling (Politis et al., 1999), showing that all estimated jumps are significant.

Table 2 reports mean squared error (MSE), jump-size bias, and misclassification rates for boundary detection, averaged over 300 (1D) and 100 (2D) simulations. All measures improve as n grows, confirming our convergence results – except for a slight and mechanical increase in the false negative rate for the jump locations due to the finer grid sizes. The false positive and negative rates for the estimated jump locations rapidly decrease to zero, indicating highly accurate jump location detection even in small samples. The estimated jump sizes for the 2D case converge to estimates that differ by less than 0.5% from the true jump sizes, except for the smallest jumps, which still converge but at a slightly slower rate. Notably, the data-driven selection of hyperparameters consistently finds $\lambda \gg \nu$, aligning with Theorem 1.

Table 2: Monte Carlo Simulations

(a) 1D

N	MSE	MSE τ_{FD}	Bias τ_{FD}	FNR	FPR
500	0.0789	0.1555	0.07	-0.0437	0.1933
1000	0.0461	0.1761	0.029	0	0.1099
5000	0.0012	0.0102	-0.0117	0	0.018

SURE: $\lambda = 98.6712$, $\nu = 0.0001$

(b) 2D

d = 0.25

N	α	$\hat{\alpha}$	MSE	MSE τ_{FD}	Bias τ_{FD}	FNR	FPR
1000	0.0377	0.0972	0.0018	0.0088	0.0595	0.0105	0.5722
5000	0.0377	0.0475	0.0011	0.0007	0.0098	0.259	0.0415
10000	0.0377	0.0445	0.0011	0.0003	0.0068	0.7593	0.0014

SURE: $\lambda = 26.0100$, $\nu = 0.0012$

d = 0.50

N	α	$\hat{\alpha}$	MSE	MSE τ_{FD}	Bias τ_{FD}	FNR	FPR
1000	0.0754	0.1059	0.002	0.0081	0.0305	0.01	0.5642
5000	0.0754	0.074	0.0012	0.002	-0.0014	0.0353	0.0499
10000	0.0754	0.0751	0.0012	0.001	-0.0003	0.0884	0.0075

SURE: $\lambda = 28.1132$, $\nu = 0.0011$

d = 0.75

N	α	$\hat{\alpha}$	MSE	MSE τ_{FD}	Bias τ_{FD}	FNR	FPR
1000	0.1131	0.1131	0.0025	0.0083	-0	0.0127	0.5126
5000	0.1131	0.1028	0.0014	0.0036	-0.0103	0.036	0.0339
10000	0.1131	0.1149	0.0013	0.0019	0.0017	0.0336	0.0074

SURE: $\lambda = 50.9836$, $\nu = 0.0014$

Note: table shows averaged results from Monte Carlo simulations of 1D and 2D (300 and 100 per row, respectively) smoothly varying functions with jumps and additive Gaussian noise ($\sigma = 0.05$) in Figures 1a and 1c. The functions have varying true jump sizes for 1D (see the notes in Figure 1) and jump sizes of Cohen's d 0.25, 0.5, 0.75 with true jump sizes indicated by α for 2D. We uniformly sample random point clouds from these functions, where N denotes the sample size, and estimate the function using our FDR estimator based on those point clouds. $\hat{\alpha}$ denotes the estimated jump size, MSE is the mean squared error with respect to the true noise-free image, $MSE \tau_{FD}$ is the MSE with respect to the true jump sizes, Bias τ_{FD} is the bias of the estimated jump sizes, FNR and FPR are the false negative and false positive rate of the estimated jump locations. Hyperparameters λ , ν are estimated using a finite-difference Monte-Carlo approximation of Stein's unbiased risk estimate (SURE) with $R = 3$ simulations on a 20×20 grid (Ramani et al., 2008), as in Eq. (5). $N = \frac{1}{20}n$ for 1D simulations, $N = \frac{2}{3}n$ for 2D simulations, where n is the raw sample size and N the number of grid cells along each dimension.

4 Application: The Economic Effects of Internet Shutdowns in India

Internet shutdowns—deliberate disruptions of internet or electronic communications—have recently drawn global attention, reaching a record high in 2022 (Rosson et al., 2023). India, with its burgeoning digital economy, has implemented at least 646 such shutdowns between 2018 and 2023 (Software Freedom Law Center, 2024), more than any other country, primarily to quell protests, communal violence, and cheating in examinations (Human Rights Watch, 2023). In this section, we exploit the geographic discontinuities caused by these shutdowns to estimate their short-term economic impact.

The FDR estimator is well-suited for this purpose because the areas exposed to the shutdown—where internet connectivity abruptly dropped—were unknown *a priori*. Its multidimensional formulation allows us to explicitly estimate the geography of the targeted areas. This is of independent interest, to understand what areas were affected, but also enables us to precisely estimate the impact of the shutdown by looking at the size of the jumps at the estimated area boundaries.

We focus on a shutdown imposed by the Rajasthan state government on September 26, 2021, to prevent cheating on the Rajasthan Eligibility Exam for Teachers. This high-stakes exam, not held since 2018, drew hundreds of thousands of candidates in 2021 amid heightened concerns of cheating after several scandals (Purohit, 2022). In the days before the exam, multiple district governments announced a mobile internet shutdown from 6 am to 6 pm.²

Several other districts also cut telecom services without notice, ultimately affecting an estimated 25 million people (Yeung et al., 2021). Because the Rajasthan telecom circle does not perfectly align with administrative boundaries, and connectivity depends on how cell towers, service providers, and mobile devices interact, it was unclear which districts—and what parts of those districts—would be affected. Where the shutdown was enforced, it was complete, as local governments compelled providers to disable both transmission (cell towers) and point-of-contact (mobile phones). This meant users could not connect to towers outside the shutdown area, inducing discontinuous drops in connectivity.

Although the shutdown technically targeted mobile services, it effectively amounted to a near-complete internet blackout. In 2022, Wi-Fi accounted for just 0.08% of wireless connectivity in India, and only 3.74% of internet subscribers had wired connections (Telecom Regulatory Authority of India, 2023). This disruption reverberated through the economy. In Jaipur alone, 80,000 shops reportedly closed (The Economist, 2021), due to the ubiquity

²Specifically, the District Magistrates or Divisional Commissioners of Ajmer, Jhunjhunu, Kota, Bundi, Baran, Jhalawar, and parts of Udaipur issued suspension orders (Mishra, 2021).

of mobile-based payment systems like UPI or Google Pay. Although cash is accepted, it is less convenient in a system where even small transactions often rely on mobile platforms (Mashal and Kumar, 2023), leading many ATMs to run dry during similar shutdowns (The Times of India, 2023). A large share of retail, hospitality, and mobile-app-based transactions also ground to a halt.

More generally, these shutdowns directly disrupt India’s digital economy, which accounted for about 22% of GDP in 2019 and continues to expand. While wired connections remained available, losing mobile connectivity still undermined supply-chain tracking, process automation, distribution networks, remote work, and customer support—especially for small and rural businesses that rely entirely on mobile internet (Kathuria et al., 2018, p.55).

A commonly cited framework for estimating the costs of internet shutdowns is the back-of-the-envelope method from West (2016),³ which uses data on the digital economy’s size, mobile penetration, and the “digital multiplier” (Quelch, 2009). While transparent, this approach does not measure actual local economic impacts, and there appear to be no academic estimates of these, despite shutdowns’ global prominence. In development economics, however, research on digital infrastructure expansions suggests notable economic benefits. Röller and Waverman (2001), for instance, found that each percentage-point rise in mobile penetration raises economic growth by around 0.15%. Other studies show welfare improvements, lower living costs, and increased employment from mobile rollouts (Jensen, 2007; Björkegren and Karaca, 2022; Couture et al., 2021; Zuo, 2021; Hjort and Poulsen, 2019), consistent with digitization reducing search, replication, transportation, tracking, and verification costs (Goldfarb and Tucker, 2019).

In contrast, an internet shutdown disrupts those welfare-improving channels, creating economy-wide ripple effects. Moreover, losing established connectivity is not simply the inverse of gaining it; digital infrastructures, once in place, play “an ‘enabling function’ across all critical infrastructure sectors” (CISA, nd). Our findings therefore complement, rather than mirror, existing work on connectivity expansions.

Lastly, using mobile device data to proxy socioeconomic activity is well-established in fields such as remote sensing, network science, and complex systems (Šćepanović et al., 2015; Kung et al., 2014; Frias-Martinez and Virseda, 2012; Eagle et al., 2010; Blumenstock et al., 2015), as well as in industry (Naef et al., 2014) and government (World Bank Group, 2022). More recently, economists and policy researchers have adopted these data to study social and economic questions (Kreindler and Miyauchi, 2021; Van Dijcke et al., 2023).

³See also Top10VPN (2023) and <https://netblocks.org/projects/cost>.

4.1 Data

We analyze anonymized device-level location data from data provider Veraset to assess the effects of the shutdown at a fine spatio-temporal granularity. The data consist of “pings”, timestamped GPS locations shared by mobile devices with apps that use common software development kits. Inside our sample area around Rajasthan, we observe 126 million unique pings from 3.8 million devices during the four Sundays of September 2021 between 6 am and 6 pm, the shutdown time window. To capture the disruption to mobile connectivity, we define

$$(6) \quad \overline{Pings}_i := \frac{Pings_{it_0}}{\frac{1}{3} \sum_{t=t_0-3}^{t_0-1} Pings_{it}},$$

where i indexes a 5×5 km grid cell overlaid on Rajasthan; t_0 indexes September 26, 2021, between 6 am and 6 pm (the shutdown period); and $t_0 - 3, \dots, t_0 - 1$ index the same time window on the three previous Sundays. $Pings_{it}$ counts mobile device pings in grid cell i in period t . The normalization by the prior month’s Sunday average removes regional differences in absolute activity levels.

To estimate economic effects, we compute an analogous measure \overline{Econ}_i that captures activity around commercial points of interest (POIs). We combine two datasets — SafeGraph Places (global retail chains) and OpenStreetMap (local businesses) — to identify approximately 108,000 retail, commercial, and industrial locations (see Appendix B for detailed classifications). We classify a ping as economically relevant if it originates within 150 meters of a POI. The economic measure is cast onto a coarser 40×40 km grid intersected with municipalities to ensure sufficient observations per cell.

Some devices continue emitting signals during the shutdown because location data is determined via satellite connections, which were unaffected. Apps with background location permissions cache these positions for later transmission, enabling measurement of economic activity even in shutdown areas. The representativeness of this cached location data and additional robustness checks are discussed in Appendix B.

4.2 Results

We apply the FDR estimator to the data described above, starting with the mobile device signal in Figure 2.

Mobile signal The raw data (Figure 2a) shows a stark drop-off in signal that aligns with the Rajasthan state boundary, with an unexpected pocket of activity in the northwest

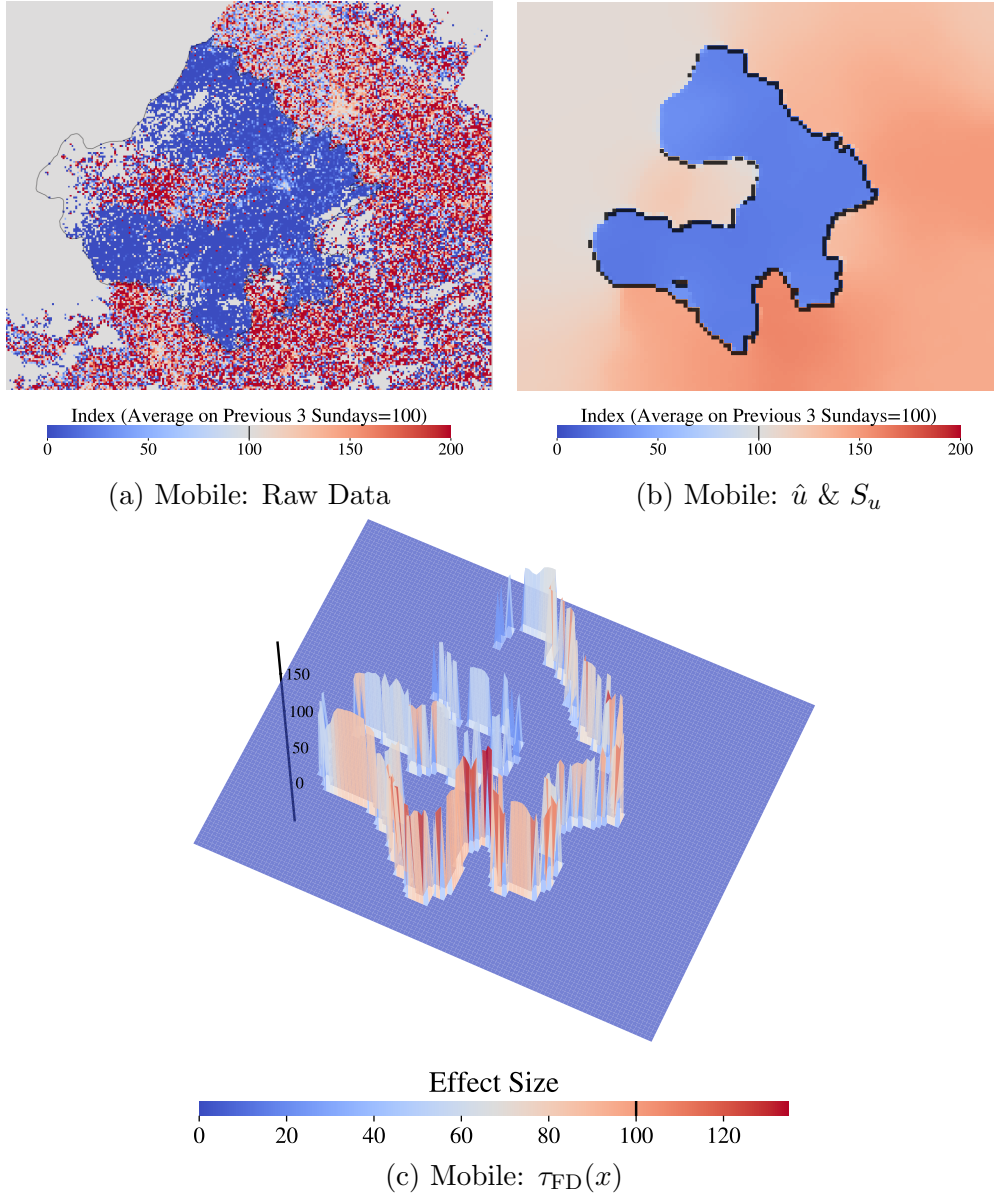


Figure 2: Internet Shutdown: Mobile Data Effects

Notes: Plots depict in- and outputs of FDR estimation of effects of internet shutdown in Rajasthan state, India, on September 26, 2021, on mobile device signal, as measured by \overline{Pings}_i (see (6)) which is a measure of the total mobile device pings per 5×5 km between 6 am and 6 pm on the day of the shutdown relative to the average in the same time window on the preceding 3 Sundays. $\lambda = 91.2474, \nu = 0.0656$ selected by SURE. (a) Shows the raw input data with the fill color of each cell indicating the value of \overline{Pings}_i . The outline of Rajasthan state is indicated by black lines. (b) shows the estimated regression function in color, with the estimated jump set S_u indicated in black. (c) shows the effect curve $\tau_{FD}(x)$ for those areas that have a jump induced by the shutdown (dropping the discontinuity in the north-east), with the z-axis indicating the magnitude of the drop in terms of \overline{Pings}_i .

intersecting the districts of Jaisalmer, Jodhpur, and Nagaur. Areas without prior signal are normalized to 100, while areas unaffected by the shutdown show signals averaging 130% of the Sunday September average. This reflects both mechanical noise from low spatial granularity and the broader economic recovery in India at that particular time in the COVID-19 pandemic (Bhaduri, 2021).

For hyperparameter selection, we search over $\lambda \in [1, 100]$ and $\nu \in [0.001, 0.1]$ to account for the large amount of noise in the mobile data. We winsorize at the 90th percentile to handle outliers from temporary gatherings and set f_X to the uniform distribution after verifying robustness to alternatives. The resulting regression function \hat{u} (Figure 2b) is smooth within the two partitions, with the estimated jump set S_u precisely capturing the state boundary and the unexpected area of continued connectivity within the state. The effect curve (2c) shows an average reduction in mobile signal of 100% relative to baseline, with higher reductions near Gujarat and Madhya Pradesh. About 25% of the baseline signal remains inside the shutdown area due to satellite-based location caching, enabling our subsequent economic analysis. Overall, we estimate that the shutdown was highly effective in its goal of disrupting connectivity, inducing a large drop in the mobile device signal throughout the targeted area.

Economic activity Figure 3 shows the results for economic activity. We construct 95% confidence bands around the function gradient using 200 subsamples at 4 different subsample sizes, estimating a convergence rate of approximately \sqrt{n} . Hyperparameters are selected from $\lambda \in [1, 5]$ and $\nu \in [0.075, 0.15]$, adjusted for the coarser grid. Despite lower resolution, the estimated jump set closely tracks the mobile signal discontinuities, overlapping with state boundaries and identifying the northwestern pocket of connectivity.

The shutdown reduced economic activity by approximately 35% in the eastern region and 60% in the western region, though the western estimate is less reliable due to sparse data and proximity to Pakistan. Outside the shutdown area, activity increased 0-5%, consistent with India’s broader economic recovery at the time (Woloszko, 2020). Scaling our estimate by 0.7—the most conservative estimate of mobility-GDP correlation from the literature (Dong et al., 2017; Frias-Martinez and Virseda, 2012; Spelta and Pagnottoni, 2021)—yields a 25% reduction in economic activity. This substantially exceeds previous estimates of shutdown costs, which predicted impacts around 16.4% of annualized GDP.

This discrepancy likely reflects two factors: previous estimates focused narrowly on digitized economic activity, missing spillovers to non-digital sectors, and relied on outdated digital economy multipliers from 2009 (Quelch, 2009) that understate digital infrastructure’s current importance, particularly in rapidly digitalizing economies like India.

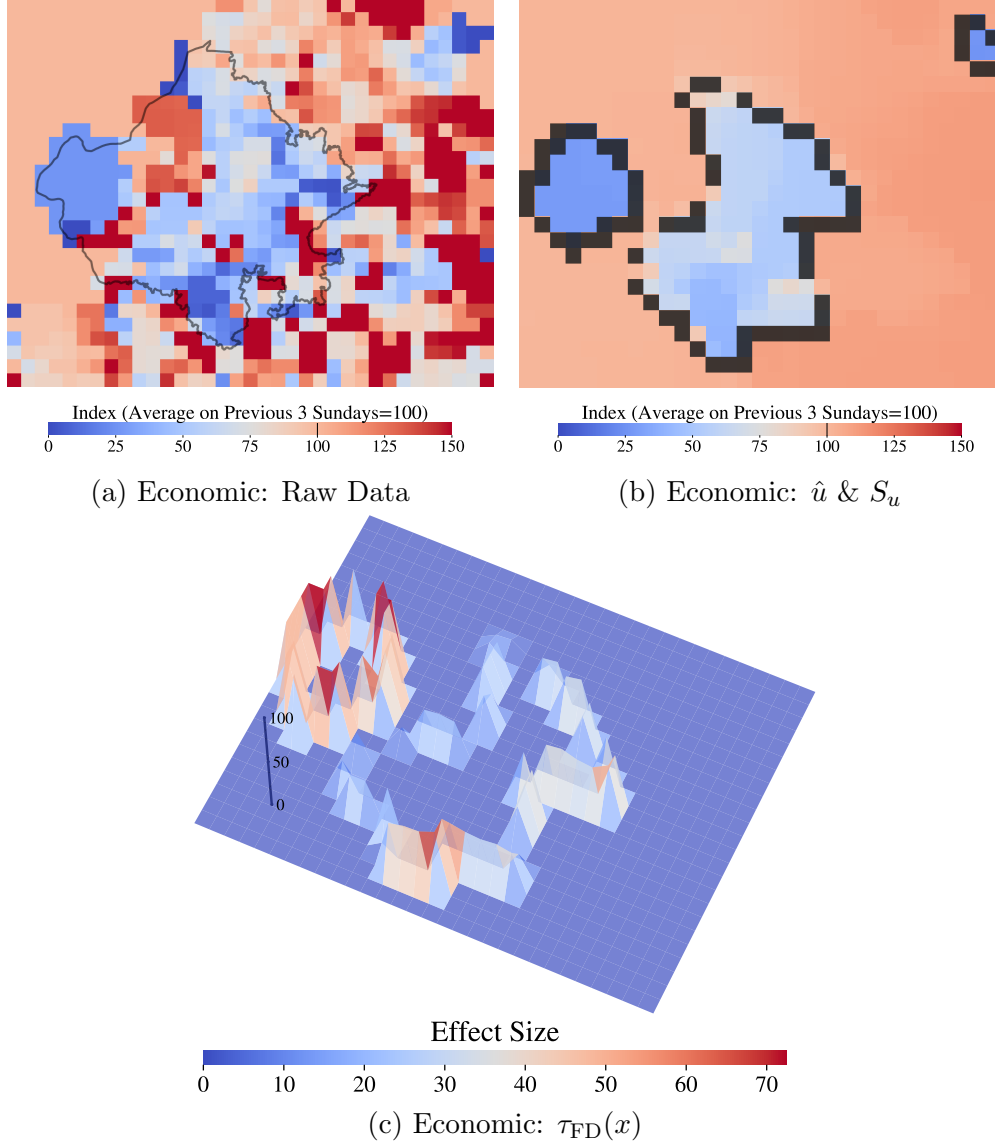


Figure 3: Internet Shutdown: Economic Effects

Notes: Plots depict in- and outputs of FDR estimation of effects of internet shutdown in Rajasthan state, India, on September 26, 2021, on economic activity, as measured by \overline{Econ}_i (see the “Economic Activity” paragraph) which is a measure of the share of mobile device pings per 40×40 km that fell within a 150m radius of a commerce-related Point of Interest between 6 am and 6 pm on the day of the shutdown relative to the average in the same time window on the preceding 3 Sundays. $\lambda = 4.9813, \nu = 0.0754$ selected by SURE.

(a) Shows the raw input data with the fill color of each cell indicating the value of \overline{Econ}_i . The outline of Rajasthan state is solid black. **(b)** shows the estimated regression function in color, with the estimated jump set S_u indicated in black if the jump size is significantly different from 0 at the 95% level based on 4×200 subsamples with estimated rate of convergence of approx. \sqrt{n} (Politis et al., 1999) and grey otherwise. **(c)** shows the effect curve $\tau_{FD}(x)$ for those areas that have a jump induced by the shutdown (dropping the discontinuity in the north-east), with the z-axis indicating the magnitude of the drop in terms of \overline{Econ}_i .

Implications Our results reveal that arbitrary internet shutdowns inflict larger short-term economic damage than previously understood. While some recovery might occur—though we find no evidence of this in mobile or economic activity the following day (Figure A-4)—the magnitude of our estimates underscores digital infrastructure’s critical role in modern economies. The findings highlight an important asymmetry: while the benefits of expanding internet access accrue gradually, the costs of removing it are immediate and substantial once digital infrastructure becomes integrated into economic activity. This emphasizes not just the importance of expanding internet access, but of ensuring its continued reliability (United Nations High Commissioner for Human Rights, 2022).

5 Conclusion

We introduced *Free Discontinuity Regression* (FDR): the first fully non-parametric framework that *simultaneously* estimates a multivariate regression surface and the geometry—and magnitude—of its unknown discontinuities. Built on a statistical reinterpretation of the convexified Mumford–Shah functional, FDR overcomes three long-standing bottlenecks in high-dimensional jump surface estimation:

1. *Unified estimation.* Unlike wavelet, fused-lasso, or post-hoc thresholding approaches, FDR brings smoothing and segmentation under a single objective, producing jump locations and sizes *as native outputs* rather than after-thoughts.
2. *Global optimality with guarantees.* Calibrations convert the non-convex Mumford–Shah functional into a saddle-point problem that primal–dual algorithms solve to *global* optimality. We prove that, under mild SBV-regularity, the recovered surface and jump set are identified and consistent in any dimension.
3. *Realistic data-generating processes.* FDR allows a random design, spatially-correlated noise, and randomness in both grid *and* sampling error—assumptions that match modern geospatial, imaging and remote-sensing datasets but are absent from existing theory.

A data-driven version of Stein’s Unbiased Risk Estimate selects the two tuning parameters automatically and in a way that is consistent with our identification theorems. Large-scale simulations from 1D to 3D confirm the predicted convergence of both surfaces and jump sizes, while an application to internet shutdowns in India showcases FDR’s empirical power—revealing a 25–35% drop in economic activity, far larger than headline estimates. This points to a large asymmetry in the effects of internet expansions and shutdowns, underscoring the internet’s critical role in modern economies.

Outlook By combining theoretical guarantees with efficient optimization procedures, the proposed estimator provides a robust and practical statistical estimation tool for multivariate changepoint estimation. Immediate extensions include (i) dynamic or panel settings where jump surfaces evolve over time, through vectorial coupling of the multiple output channels (Strekalovskiy et al., 2012), (ii) adaptive or multiresolution grids for ultra-high-resolution imagery, (iii) instrumental-variable and causal designs that leverage the estimated discontinuity set as an endogenous boundary, and (iv) computational improvements through statistical versions of the sublabel-accurate approaches in the image literature (Mollenhoff and Cremers, 2017). The hope is that the framework will spur new research into the estimation and application of jumps in high-dimensional processes and further bridge the gap between computer vision and statistical estimation.

The supplementary material introduces the mathematical notation (A), additional details on the empirical application (B), detailed proofs of the results in the texts (C), implementation details (D), details on uncertainty quantification (E), and additional results (F).

Appendices

Appendix A Mathematical Notation and Definitions

This section contains notation and definitions of mathematical objects used in the main text. These are standard and we refer to [Ambrosio et al. \(2000\)](#) for further reading.

Definition 2 (Approximate jump points). *Let u be locally integrable on \mathcal{X} , that is $u \in L^1_{loc}(P_X)$, where P_X denotes the law of X . We say that a point $x \in \mathcal{X}$ is an approximate jump point of u if there exist constants $a, b \in \mathbb{R}$ and an orientation $\rho \in \mathbb{S}^{d-1}$ such that $a \neq b$ and*

$$(7) \quad \lim_{\varepsilon \downarrow 0} \frac{\int_{B_\varepsilon^+(x, \rho)} |u(x') - a| dP_X(x')}{P_X(B_\varepsilon^+(x, \rho))} = 0, \quad \lim_{\varepsilon \downarrow 0} \frac{\int_{B_\varepsilon^-(x, \rho)} |u(x') - b| dP_X(x')}{P_X(B_\varepsilon^-(x, \rho))} = 0,$$

where

$$\begin{cases} B_\varepsilon^+(x, \rho) := \{x' \in B_\varepsilon(x) : \langle x' - x, \rho \rangle > 0\} \\ B_\varepsilon^-(x, \rho) := \{x' \in B_\varepsilon(x) : \langle x' - x, \rho \rangle < 0\} \end{cases}$$

denote the two half balls, oriented by ρ , contained in the ε -ball $B_\varepsilon(x)$, and \mathbb{S}^{d-1} is the unit sphere in \mathbb{R}^d . The triplet (a, b, ρ) , uniquely determined by (7) up to a permutation of (a, b) and a change of sign of ρ , is denoted by $(u^+(x), u^-(x), \rho_u(x))$; with u^+, u^- called the traces of u . The approximate discontinuity set contains all approximate jump points and is denoted by S_u .

A Radon measure μ is an inner regular and locally finite Borel measure. We denote

$$\int_A f(x) d\mu(x) := \frac{\int_A f(x) d\mu(x)}{\mu(A)}.$$

We denote the space of (k -times) continuously differentiable functions on \mathcal{X} by $C^k(\mathcal{X})$. $C_0(\mathcal{X})$, the space of all continuous functions that vanish eventually, is the closure in the sup-norm of $C_c(\mathcal{X})$, the space of all continuous functions on \mathcal{X} with compact support.

The k -dimensional Hausdorff-measure $\mathcal{H}^k(A)$ of a set $A \subset \mathbb{R}^d$, for $k \in [0, +\infty)$, is defined

as (e.g. [Ambrosio et al., 2000](#), Definition 2.46)

$$\mathcal{H}^k(A) := \lim_{\delta \downarrow 0} \frac{\pi^{k/2}}{2^k \Gamma(1 + k/2)} \inf \left\{ \sum_{i \in I} (\text{diam}(A_i))^k : \text{diam}(A_i) < \delta, A \subset \bigcup_{i \in I} A_i \right\}$$

with $\Gamma(x)$ being Euler's Gamma function, $\text{diam}(A)$ the diameter of the set A , and where the sums are taken over finite or countable covers of A .

We use the following definition of functions of bounded variation.

Definition 3 (Functions of bounded variation and SBV). ([Ambrosio et al., 2000](#), Def. 3.1) Let $u \in L^1(\mathcal{X})$; we say that u is a function of bounded variation in $\mathcal{X} \subset \mathbb{R}^d$ if the distributional derivative of u , Du , is representable by a finite Radon measure in \mathcal{X} . i.e. if

$$(8) \quad \int_{\mathcal{X}} u \operatorname{div} \varphi dx = - \sum_{i=1}^d \int_{\mathcal{X}} \varphi_i dD_i u \quad \forall \varphi \in C_c^1(\mathcal{X}).$$

for some \mathbb{R}^d -valued Radon measure $Du = (D_1 u, \dots, D_d u)$ in \mathcal{X} and all continuously differentiable test functions φ . The vector space of all functions of bounded variation in \mathcal{X} is denoted by $BV(\mathcal{X})$. If the Cantor part $D_c u$ of the decomposition of Du is zero, then u is called a special function of bounded variation and denoted as $u \in SBV(\mathcal{X})$.

We define the weak*-topology in the standard way ([Ambrosio et al., 2000](#), Definition 3.11): Consider some $u \in BV(\mathcal{X})$ and a sequence $\{u_n\} \subset BV(\mathcal{X})$. Then we say that $\{u_n\}$ converges to u in the weak*-topology, or $u_n \xrightarrow{*} u$, if u_n converges to u in $L^1(\mathcal{X})$ and the corresponding Du_n converge in the weak*-topology to Du , i.e.

$$\lim_{n \rightarrow \infty} \int_{\mathcal{X}} \phi dD u_n = \int_{\mathcal{X}} \phi dD u \quad \text{for all } \phi \in C_0(\mathcal{X}).$$

For two non-empty subsets $A, B \subset M$ of some metric space (M, d) , we define their Hausdorff distance as

$$d_H(A, B) := \max \left\{ \sup_{a \in A} \operatorname{dist}(a, B), \sup_{b \in B} \operatorname{dist}(b, A) \right\},$$

where $\operatorname{dist}(a, B) := \inf_{b \in B} d(a, b)$ is the distance of a from B .

Appendix B Data and Measurement

Anonymized device-level location data from data provider Veraset allow us to assess the effects of the shutdown at a fine spatio-temporal granularity. The data consist of "pings",

timestamped GPS locations shared by the device with a mobile app. Veraset cleans and aggregates such data from thousands of "Software-Development Kits" (SDK), packages of tools that supply the infrastructure for most mobile applications. Location data from the same device can be recombined from various SDKs by use of an anonymized device ID. Inside our sample area, which is a bounding box around the state of Rajasthan, we observe 126 million unique pings on the four Sundays of September 2021 between 6 am and 6 pm, emanating from 3.8 million unique devices. With an estimated smartphone penetration of 60.63% in India in 2021 and a population in Rajasthan of around 80 million, this means we capture a little under 10% of all mobile devices in the area.

Few other data sources can proxy for economic activity at the fine spatiotemporal granularity we consider: night lights data are not suited for such rapid temporal variations in economic activity that happen during daytime; credit card penetration is low in India (around 5%); and data from neither Google Pay nor UPI were being sold to third parties at the time of this paper's writing.

Our device-based measure should be a good proxy of economic activity under two assumptions: 1) the economic activity of the restricted device sample is representative of the wider population; 2) the set of apps that cached devices' background location for the duration of the shutdown was not in some way skewed so as to collect geolocation information at different rates in economic areas during the shutdown. To point 1), though information on location-sharing behavior by Indian smartphone users is sparse, one recent poll of Android users suggests 66.78% have background location enabled, and Android makes up 95.21% of the smartphone market share in India ([Android Authority, 2022](#); [Statcounter, 2023](#)). This is further supported by the fact that even after filtering on economic areas for our restricted device sample, we still retain around 68 million unique pings compared to the 126 million total pings. To point 2), our location data comes from 1,000+ different mobile applications which allows location tracking across a wide variety of platforms and thus areas and behaviors. Additionally, background location collection happens continuously so it should not be meaningfully affected by people's differential app usage during the shutdown.

One might expect there to be selection effects on economic activity around the discontinuity, if people near the border cross state lines to avoid the shutdown. We can test for such selection effects by counting the number of devices that are observed crossing the state boundaries during the shutdown and comparing it to the average in the preceding month. We focus on a 40km band around the Rajasthan state boundary as illustrated in [Figure A-3](#). We calculate the share of devices near the boundary that appeared in one of the neighboring states during the shutdown period and compare this share to its average in the month prior.

We find that 2.66% of devices near the discontinuity cross it between 6 am and 6 pm on

the day of the shutdown, while on average 3.57% do so in the same time window the month prior. Thus, there do not appear to be any self-selection effects associated with the localized internet shutdown. In fact, the lower share of devices that cross suggests that some crossing behavior was disrupted due to the shutdown, likely because of the associated disruption of mobile-based navigation services. This does not contradict the fact that location apps may still be caching devices' location, as route calculation and live navigation require full mobile connection, not just satellite-based geo-positioning. Relatedly, we do not expect mobile phones near the Rajasthan border to connect to telecommunications masts across the border, as the shutdown was implemented at the point of contact (the mobile phone) and not just the transmission points (the masts), as mentioned in the main text.

Appendix C Proofs

C.1 Proof of Proposition 1

Proof. We work in the weak*-topology (Ambrosio et al., 2000, Definition 3.11). Since all v have a uniformly bounded variation by $c < +\infty$ and since all v map to $[0, 1]$ and are hence uniformly bounded, it follows from Theorem 4.8 in Ambrosio et al. (2000) that $C \cap \{v : |Dv| \leq c\}$ is compact in the weak*-topology.

Now we want to prove that the objective function $E(v)$ is lower semi-continuous in v . For this, we analyze the inner optimization problem. Since C_0 is a Banach space with respect to the supremum norm, Corollary 6.40 in Aliprantis and Border (2006) implies that the objective function of (3) is jointly continuous as the total variations are bounded by $c < +\infty$. Moreover, the constraint set K does not depend on v , so it is trivially upper hemicontinuous in v . Therefore, Lemma 17.29 in Aliprantis and Border (2006) proves that $E(v)$ is lower semicontinuous in v . Thus, the optimization problem $\inf_{v \in C \cap \{v : |Dv| \leq c\}} E(v)$ admits a minimizer in C , which shows existence. The fact that the solution is a global minimum follows from the convexity of $C \cap \{v : |Dv| \leq c\}$. \square

C.2 Proof of Theorem 1

Proof. We first show that if we set $v^*(x, t) = \mathbb{1}_f(x, t)$, then $E(v^*) < +\infty$ for any $\lambda \geq 0$ and also as $\lambda \rightarrow +\infty$. In fact, since $f \in SBV(\mathcal{X})$ by assumption, fixing the rotation via the inward normal to the graph, the objective function in (3) can be written as (Alberti et al.,

2001, Lemma 2.10)

$$E(\mathbf{1}_f) = \sup_{p \in K} \int_{\mathcal{X}} [p^x(x, f(x)) \cdot \nabla f(x) - p^t(x, f(x))] dx + \\ \int_{S_f} \left[\int_{f^-}^{f^+} p^x(x, t) dt \right] \cdot \rho_f(x) d\mathcal{H}^{d-1}(x),$$

where p^x denotes the first d dimensions of the vector field p and p^t denotes the lifted dimension. $f^-(x)$ and $f^+(x)$ denote the respective traces corresponding to the inward normal orientation $\rho_f(x)$ of the graph of f at the point $x \in S_f$. Note that when using $f(x)$, the constraint set K implies under Assumption 1 that

$$p^t(x, f(x)) \geq \frac{|p^x(x, f(x))|^2}{4f_X(x)} \geq 0$$

independently of λ and ν . Moreover, by Assumption 1 it holds that $\int_{\mathcal{X}} |\nabla f|^2 dx < +\infty$. This, by an application of Hölder's inequality for vector-valued functions in conjunction with the fact that $p \in K$ – and thus p^t cannot be negative – and $\nu < +\infty$ implies that the first term on the right-hand side is finite for all $p \in K$. For the second term on the right-hand side note that by assumption $\mathcal{H}^{d-1}(S_f) < +\infty$. Furthermore, since $p \in K$, the integrand over $p^x(x, t)$ is bounded by $\nu < +\infty$, so that the overall $E(\mathbf{1}_f) < +\infty$ for all $\lambda \geq 0$ and also as $\lambda \rightarrow +\infty$.

We now show that in the limit as $\lambda \rightarrow +\infty$ and for fixed $\nu > 0$, it holds that $\nabla v^*(\lambda) = 0$ \mathcal{L}^{d+1} -almost everywhere. To prove this, consider any $v \in C$. Since $v \in SBV(\mathbb{R}^{d+1})$ it holds by definition that

$$Dv = \nabla v \mathcal{L}^{d+1} + (v^+ - v^-) \rho_v \mathcal{H}^d \llcorner J_v,$$

where J_v is the set where $v(x, t)$ jumps, ρ_v is a corresponding orientation, and \mathcal{L}^{d+1} denotes the $(d+1)$ -dimensional Lebesgue measure. Note that by the Federer-Vol'pert theorem (Ambrosio et al., 2000, Theorem 3.78) J_v coincides with S_v \mathcal{H}^d -almost everywhere, so that we focus on J_v . It therefore holds that

$$\int p \cdot Dv = \int p \cdot \nabla v d\mathcal{L}^{d+1} + \int_{J_v} (v^+ - v^-) p \cdot \rho_v d\mathcal{H}^d.$$

Since $v \in C$, it cannot be constant everywhere because the limits as $t \rightarrow \pm\infty$ are different for all $x \in \mathcal{X}$. On the other hand, as $\lambda \rightarrow +\infty$, the range of p^t converges to \mathbb{R} , which implies that for every $\eta > 0$ and every $v \in C$ such that $\nabla v \neq 0$ on a subset of \mathbb{R}^{d+1} of positive \mathcal{L}^{d+1} -measure, there exists a large enough λ and a corresponding $p \in K$ such that

$\int p \cdot \nabla v \, dx > \eta$. This implies that no v for which ∇v is not constant on a set of positive \mathcal{L}^{d+1} measure can be a solution to (3) as $\lambda \rightarrow +\infty$. Therefore, in the limit as $\lambda \rightarrow +\infty$, the only changes in v must lie in J_v .

We now prove the rest of the theorem. First, we prove that if $v \in C$ is such that for some $\eta > 0$

$$(9) \quad \Gamma_f \not\subset J_v^\eta(\lambda),$$

where $A^\eta := \{x' \in \mathcal{X} : \text{dist}(x', A) \leq \eta\}$ is the η -enlargement of A , then it cannot be a solution to (3) in the limit as $\lambda \rightarrow +\infty$. Then we prove that if for some $\eta > 0$

$$(10) \quad J_v(\lambda) \not\subset \Gamma_f^\eta$$

then it cannot be a solution to (3) in the limit as $\lambda \rightarrow +\infty$.

Showing (9) leads to a contradiction.

The idea is to show that $\lim_{\lambda \rightarrow +\infty} E(v(\lambda)) = +\infty$ for any sequence $\{v(\lambda)\} \subset C$ that satisfies (9). So suppose that $\{v(\lambda)\} \subset C$ is some sequence that satisfies (9). This implies that in the limit as $\lambda \rightarrow +\infty$, it holds that there is some $(x', t') \in \Gamma_f$ such that $\text{dist}((x', t'), J_v(\lambda)) > \eta > 0$.

This can happen in two ways. Either, $x' \notin S_f$ or $x' \in S_f$. Recall that under the first part of Assumption 2 it holds that $\mathcal{H}^{d-1}(\bar{S}_f \setminus S_f) = 0$, where \bar{S}_f is the closure. We now consider each case one by one.

First subcase. In the first case, it follows that there is some $\delta > 0$ such that $\text{dist}(x', S_f) > \delta$. We now use the Lipschitz assumption on f to show that $\mathcal{H}^d(\Gamma_f \setminus J_v) > 0$. In fact, it holds that $B_\delta(x') \cap S_f = \emptyset$. Now by the second part of Assumption 2 there exists a Lipschitz constant $L < +\infty$ such that

$$|f(x') - f(x'')| \leq L|x' - x''| \leq L\delta$$

for all $x'' \in B_\delta(x') \subset \mathcal{X}$. Now we pick $\delta > 0$ small enough such that the set $Z := B_\delta(x') \times B_{L\delta}(f(x'))$ has diameter η . The diameter of Z is $\text{diam}(Z) = \delta\sqrt{2 + L^2}$, so that if we define $\delta < \frac{\eta}{\sqrt{2 + L^2}}$, then $\text{diam}(Z) < \eta$. We can do this under Assumption 2. This implies in particular that $Z \cap J_v = \emptyset$.

Now the fact that $\mathcal{H}^d(Z \cap \Gamma_f) = \mathcal{H}^d((Z \cap \Gamma_f) \setminus J_v) > 0$ follows from an application of the area formula since Γ_f is a Lipschitz graph. In fact, we get (e.g. Ambrosio et al., 2000,

p. 88)

$$\mathcal{H}^d(Z \cap \Gamma_f) = \int_{B_\delta(x')} \sqrt{1 + |\nabla f|^2} \, d\mathcal{L}^d > 0.$$

Denote

$$W := \{(x, t) \in J_v : x \in B_\delta(x')\}.$$

We have just shown that J_v does not contain $Z \cap \Gamma_f$ on a set $B_\delta(x')$ of positive d -dimensional Hausdorff measure, which implies that for \mathcal{H}^d -almost every $(x, t) \in W$, $t \neq f(x)$. Moreover, by definition $|v^+(x, t) - v^-(x, t)| > 0$ for \mathcal{H}^d -almost all $(x, t) \in J_v$. Since $f \in SBV(\mathcal{X})$ it holds by definition that J_v is measurable with respect to \mathcal{H}^d . Therefore,

$$(11) \quad \lim_{\lambda \rightarrow +\infty} \sup_{p \in K} \int_{J_v} (v^+ - v^-) p \cdot \rho_v \, d\mathcal{H}^d \\ = \lim_{\lambda \rightarrow +\infty} \sup_{p \in K} \left[\int_W (v^+ - v^-) p \cdot \rho_v \, d\mathcal{H}^d + \int_{J_v \setminus W} (v^+ - v^-) p \cdot \rho_v \, d\mathcal{H}^d \right].$$

Now note that it must hold that $\mathcal{H}^d(W) > 0$. In fact, since $v \in SBV(\mathcal{X} \times \mathbb{R})$, it holds that J_v is countably \mathcal{H}^d -rectifiable (e.g. [Ambrosio et al., 2000](#), chapter 4). Since $B_\delta(x')$ is compact, W is also compact. This directly implies by Proposition 2.66 in [Ambrosio et al. \(2000\)](#) that $\mathcal{H}^d(W) \geq \mathcal{L}^d(\pi_{\mathcal{X}}(W))$, where $\pi_{\mathcal{X}}$ is the projection onto \mathcal{X} . But $\pi_{\mathcal{X}}(W) = B_\delta(x')$, which is of positive \mathcal{L}^d measure. The first term on the right hand side of (11) diverges to $+\infty$ because the range of p^t increases to \mathbb{R} as $\lambda \rightarrow +\infty$ and $t'' \neq f(x'')$ for \mathcal{L}^d -almost every $x'' \in B_\delta(x')$. This implies that such a v cannot be a solution to (3) in the limit as $\lambda \rightarrow +\infty$.

Second subcase. We now suppose $x \in S_f$. Since $x \in S_f$, we now have to work with the points $(x, f^+(x))$ and $(x, f^-(x))$. Without loss of generality focus on the former and suppose that $\text{dist}((x, f^+(x)), J_v(\lambda)) > \eta$ for all $\lambda > 0$ and as $\lambda \rightarrow +\infty$. By Assumption 1, we know that $\mathcal{H}^{d-1}(S_f) < +\infty$, so that (e.g. [Mattila, 1999](#), Theorem 4.7) $\mathcal{L}^d(S_f) = 0$ on \mathcal{X} . The first part of Assumption 2 implies that $\mathcal{L}^d(\bar{S}_f) = 0$ since it implies $\mathcal{H}^{d-1}(\bar{S}_f \setminus S_f) = 0$. This further implies that the projection $\pi_{\mathcal{X}}(B_\eta((x, f^+(x))))$ is such that it intersects $\mathcal{X} \setminus \bar{S}_f$ in such a way that

$$\mathcal{L}^d(\pi_{\mathcal{X}}(B_\delta((x, f^+(x)))) \cap (\mathcal{X} \setminus \bar{S}_f) > 0.$$

Moreover, by Assumption 2 we know that $f(x)$ is Lipschitz away from \bar{S}_f , which directly implies that there must be points $(x', f(x'))$ in $B_\delta((x, f^+(x)))$ with $\text{dist}((x', f(x')), J_v) > 0$. This brings us back to the first subcase above and we can derive a contradiction this way and proves that (9) cannot be a solution in the limit as $\lambda \rightarrow +\infty$.

Showing (10) leads to a contradiction.

Suppose (10) holds and denote $Z^\eta := J_v \setminus \Gamma_f^\eta$ for some fixed $\eta > 0$. By our assumption, we know that Z^η is not empty, so there is some $(x, t) \in (\mathcal{X} \times \mathbb{R}) \cap Z^\eta$. As before J_v must be countably \mathcal{H}^d -rectifiable since $v \in SBV(\mathcal{X} \times \mathbb{R})$. This implies (e.g. [Mattila, 1999](#), Lemma 15.5 (2)) that Z^η is countably \mathcal{H}^d -rectifiable. One direction of a theorem based on results by Besicovitch-Marstrand-Mattila ([Ambrosio et al., 2000](#), Theorem 2.63) implies that

$$\theta_d(Z^\eta, (x, t)) = 1 \quad \mathcal{H}^d\text{-almost every } (x, t) \in \mathcal{X} \times \mathbb{R},$$

where

$$\theta_d(A, y) := \liminf_{r \downarrow 0} \frac{\mathcal{H}^d(B_r(y))}{\omega_d r^d}$$

is the lower density of the Hausdorff measure with respect to the volume of the d -dimensional unit ball ω_d . We may hence assume that there exist some $r_0 > 0$ and $c > 0$ such that

$$\mathcal{H}^d(Z^\eta \cap B_r((x, t))) \geq cr^d, \quad (x, t) \in Z, \quad 0 < r < r_0.$$

Recall that for any $(x, t) \in Z^\eta \cap B_r((x, t))$ it must hold that $t \neq f(x)$. Since Z^η is by definition \mathcal{H}^d -measurable, it holds by the same argument as in (11) that

$$(12) \quad \begin{aligned} & \lim_{\lambda \rightarrow +\infty} \sup_{p \in K} \int_{J_v} (v^+ - v^-) p \cdot \rho_v \, d\mathcal{H}^d \\ &= \lim_{\lambda \rightarrow +\infty} \sup_{p \in K} \left[\int_{Z^\eta \cap B_r((x, t))} (v^+ - v^-) p \cdot \rho_v \, d\mathcal{H}^d + \int_{J_v \setminus (Z^\eta \cap B_r((x, t)))} (v^+ - v^-) p \cdot \rho_v \, d\mathcal{H}^d \right]. \end{aligned}$$

Now focus on the first term on the right and recall that we only consider the limit as $\lambda \rightarrow +\infty$. Hence, for every constant $M > 0$ and every $r > 0$ there exists $\lambda > 0$ such that the first term on the right hand side of (12) is greater than M . This means that the first term on the right hand side of (12) diverges to $+\infty$ as $\lambda \rightarrow +\infty$ because we can always pick a large enough λ for every r and because the range of p^t increases to \mathbb{R} as $\lambda \rightarrow +\infty$, and $t \neq f(x)$ for every $(x, t) \in Z$. This shows the contradiction to (10) for every $\eta > 0$ and proves that $\lim_{\lambda \rightarrow +\infty} d_H(J_v, \Gamma_f) = 0$ for λ that diverges fast enough. \square

C.3 Proof of Proposition 2

We now proof convergence for a *deterministic* analogue of the problem, for which the estimators \hat{f}_{Nn} and $\hat{f}_{X,h(n)}$ are known functions whose values are given in the center of each pixel. We do this for two reasons. First, it clarifies the proof for the statistical setting. Second, it provides a novel convergence result in the mathematical literature on image recognition,

complementing recent convergence results (Caroccia et al., 2020; Chambolle and Pock, 2021; Ruf, 2019). Throughout, we assume that $v \in [0, 1]^{d+1}$ without loss of generality since all functions are defined on a compact subset of \mathbb{R}^{d+1} by Assumption 3.

To prove Proposition 2, we require a lemma, which relates the discrete problem to the approximation of the continuous problem via cubes. In the following, and to lighten the notational burden in proofs, we define

$$v_{k_1, \dots, k_j, \dots, k_{d+1}}^\uparrow := v_{k_1, \dots, k_j+1, \dots, k_{d+1}}$$

the forward value of $v_{k_1, \dots, k_j, \dots, k_{d+1}}$ for a given dimension k_j . As in the main text, we write $k := k_1, \dots, k_{d+1}$, and hence $v_k := v_{k_1, \dots, k_{d+1}}$. We write v_k^j if we want to emphasize one specific dimension $j = 1, \dots, d+1$, otherwise the dimension is defined by the context.

Lemma 1. *For the empirical analogues Dv_N of Dv and p_N of p as defined in the main text, it holds that*

$$\int_{[0,1]^{d+1}} p \cdot Dv_N = \frac{1}{N^{d+1}} \langle p_N, D_N v_N \rangle_N,$$

with

$$\langle p_N, D_N v_N \rangle_N = \sum_{0 \leq k_1, \dots, k_{d+1} \leq N} N \left(v_{k_1, \dots, k_{d+1}}^\uparrow - v_{k_1, \dots, k_{d+1}} \right) p_{k_1, \dots, k_{d+1}}^\uparrow.$$

Proof of Lemma 1. Note that $v_N \in SBV([0, 1]^{d+1})$ for all $N \in \mathbb{N}$, since it is a piecewise constant function and the partition \mathcal{Q}_N is a Caccioppoli partition by Theorem 4.16 in Ambrosio et al. (2000) in combination with Theorem 4.5.11 in Federer (2014). We can therefore write

$$\int_{[0,1]^{d+1}} p \cdot Dv_N = \sum_{0 \leq k \leq N} \int_{Q_k} p \cdot \nabla v_k \, dx + \sum_{0 \leq k \leq N} \int_{\partial Q_k^\uparrow \cap \partial Q_k} (v_k^\uparrow - v_k) p \cdot s \, d\mathcal{H}^d,$$

where the orientation $s \in \mathbb{S}^{d+1}$ is chosen in the “forward direction”, i.e. from j to $j+1$, which means that it takes the form of unit vectors $e_j \in \mathbb{R}^{d+1}$ with zeros everywhere except a 1 in one of the j positions. Since v_k is constant on Q_k it holds that $\nabla v_k = 0$ on Q_k , so that the first term vanishes.

For the second term, we have

$$\sum_{0 \leq k \leq N} \int_{\partial Q_k^\uparrow \cap \partial Q_k} (v_k^\uparrow - v_k) p_k \cdot s \, d\mathcal{H}^d = \sum_{0 \leq k \leq N} (v_k^\uparrow - v_k) p_k^\uparrow \frac{1}{N^d},$$

where we define $p_k^\uparrow = p_k \cdot e^\uparrow$, where e^\uparrow is the unit vector in the forward direction for respective j . The inequalities follow because p_k is constant on the boundary of the respective cube

where it is defined and since the Hausdorff measure of a face of the hypercube in $d + 1$ dimensions with sidelength $\frac{1}{N}$ is $\frac{1}{N^d}$. Also recall that the orientation s is in terms of forward differences, so that p_k in the above expression is the one that lies on the boundary of Q_k and the corresponding Q_k^\uparrow .

We therefore have

$$\begin{aligned} \int_{[0,1]^{d+1}} p \cdot Dv_N &= \frac{1}{N^d} \sum_{0 \leq k \leq N} \left(v_k^\uparrow - v_k \right) p_k^\uparrow \\ &= \frac{1}{N^{d+1}} \sum_{0 \leq k \leq N} N \left(v_k^\uparrow - v_k \right) p_k^\uparrow \\ &\equiv \frac{1}{N^{d+1}} \langle p_N, D_N v_N \rangle_N. \end{aligned}$$

□

With this result, we are ready to prove Proposition 2.

Proof of Proposition 2. In the following, we denote weak*-convergence by $\xrightarrow{*}$. To prove Γ -convergence we need to show (Dal Maso, 2012, Proposition 8.1)

- (i) for every $v \in C$ and every sequence $v_N \in \tilde{C}_N$ with $v_N \xrightarrow{*} v$ it holds that

$$E(v) \leq \liminf_{N \rightarrow \infty} E_N(v_N)$$

and

- (ii) for every $v \in C$ there exists a sequence $v_N \in \tilde{C}_N$ with $v_N \xrightarrow{*} v$ such that

$$E(v) \geq \limsup_{N \rightarrow \infty} E_N(v_N).$$

Part (i): Let $v_N \xrightarrow{*} v$ and assume $\liminf_{N \rightarrow +\infty} E_N(v_N) < +\infty$. Let $p \in C_c^\infty([0, 1]^{d+1}, \mathbb{R}^{d+1}) \cap K$.

As in the main text, the discrete approximation of p is achieved by decomposing $[0, 1]^{d+1}$ into hypercubes of sidelength $\frac{1}{N}$. We define $p_k^{j+\frac{1}{2}}$ as the average flux through the boundary of two adjacent hypercubes Q_k^{j+1} and Q_k^j , i.e.

$$p_k^{j+\frac{1}{2}} = N^d \int_{\partial Q_k^{j+1} \cap \partial Q_k^j} p \cdot s \, d\mathcal{H}^d,$$

where $s \in \mathbb{S}^d$ is the orientation chosen in the direction from j towards $j + 1$. We then define

$$p_N = \sum_{0 \leq k \leq N} p_k.$$

Now we need to analyze the above constructed p_N in terms of \hat{K} , which consists of two constraints. Let us start with the first. Each p_k is a $(d + 1)$ -dimensional vector, and we have to distinguish between the first d entries of this vector and the last entry. To do this, we will write p_k^x as the vector consisting of the first d entries and p_k^t as the last entry of p_k . Furthermore, for the cube Q_k we denote its centerpoint by x_k .

We can now analyze

$$(13) \quad \left| \frac{1}{N} \sum_{\kappa_1 \leq k_{d+1} \leq \kappa_2} p_k^x \right| = \left| \frac{1}{N} \sum_{\kappa_1 \leq k_{d+1} \leq \kappa_2} p_k^x + p^x(x_k) - p^x(x_k) \right| \\ \leq \left| \frac{1}{N} \sum_{\kappa_1 \leq k_{d+1} \leq \kappa_2} p_k^x - p^x(x_k) \right| + \left| \frac{1}{N} \sum_{\kappa_1 \leq k_{d+1} \leq \kappa_2} p^x(x_k) \right|$$

for $\kappa_1, \kappa_2 \in \{1, \dots, N\}$. Since p is smooth and in particular Lipschitz, we can bound the first term in terms of the Lipschitz constant and the edge length. Let $L < +\infty$ be the Lipschitz constant and note that the Euclidean distance between x_k and the center of one of the boundaries of Q_k is $\frac{1}{2N}$. We can hence bound the first term as

$$\left| \frac{1}{N} \sum_{\kappa_1 \leq k_{d+1} \leq \kappa_2} p_k^x - p^x(x_k) \right| \leq \frac{1}{N} \sum_{\kappa_1 \leq k_{d+1} \leq \kappa_2} |p_k^x - p^x(x_k)| \\ \leq \frac{1}{N} \sum_{\kappa_1 \leq k_{d+1} \leq \kappa_2} \frac{L}{2N} \\ \leq \frac{L}{2N}.$$

The second term in (13) is bounded above by $\nu + o(1)$ since $p \in K$ and a Riemann sum argument. So overall, we have

$$\frac{1}{N} \left| \sum_{\kappa_1 \leq k_{d+1} \leq \kappa_2} p_k^x \right| \leq \nu + o(1) + \frac{L}{2N}.$$

So for $p_N \in \hat{K}$ we would have to normalize each p_k^x as

$$\tilde{p}_k^x = p_k^x \frac{\nu}{\nu + o(1) + \frac{L}{2N}}.$$

Let us now analyze the second part of the constraint \hat{K} . Recall that the constraint for K reads

$$|p^x(x, t)|^2 \leq 4 (p^t(x, t) + \lambda(t - f(x))^2).$$

By Assumption 3 the term in square brackets is bounded for all t and x . We now analyze

$$|p_k^x|^2 \leq (|p_k^x - p^x(x_k)| + |p^x(x_k)|)^2,$$

where x_k is again the center point of the cube Q_k . The first term can be bounded in the same way as above:

$$|p_k^x - p^x(x_k)| \leq \frac{L}{2N}.$$

By the fact that $p \in K$ the second term satisfies

$$\begin{aligned} |p^x(x_k)| &\leq 2\sqrt{p^t(x_k) + \lambda(t_k - f(\tilde{x}_k))^2} \\ &\leq 2\sqrt{|p^t(x_k) - p_k^t| + p_k^t + \lambda(t_k - f(\tilde{x}_k))^2} \\ &\leq 2\sqrt{\frac{L}{2N} + p_k^t + \lambda(t_k - f(\tilde{x}_k))^2}, \end{aligned}$$

where we define $x_k \equiv (\tilde{x}_k, t_k) \in \mathbb{R}^{d+1}$ and the second line follows from $(a - b) \leq |a - b|$. Note that f is a bounded function by Assumption 3, which in our discretization scheme is approximated in the center of each cube. Putting both terms together gives

$$\begin{aligned} |p_k^x|^2 &\leq \left(\frac{L}{2N} + \sqrt{\frac{2L}{N} + 4(p_k^t + \lambda(t_k - f(\tilde{x}_k))^2)} \right)^2 \\ &\leq \left(\frac{L}{2N} + \sqrt{\frac{2L}{N}} + \sqrt{4(p_k^t + \lambda(t_k - f(\tilde{x}_k))^2)} \right)^2 \\ &= \left(\frac{L}{2N} + \sqrt{\frac{2L}{N}} \right)^2 + 2 \left(\frac{L}{2N} + \sqrt{\frac{2L}{N}} \right) \sqrt{4(p_k^t + \lambda(t_k - f(\tilde{x}_k))^2)} + \\ &\quad 4(p_k^t + \lambda(t_k - f(\tilde{x}_k))^2) \\ &:= C_p, \end{aligned}$$

where we used the inequality $\sqrt{a+b} \leq \sqrt{a} + \sqrt{b}$ in the second line.

So in order to make $\tilde{p}_N \in \hat{K}_N$, we would need to normalize

$$\tilde{p}_k^x = p_k^x \left(\frac{\nu}{\nu + o(1) + \frac{L}{2N}} \right) \quad \text{and} \quad \tilde{p}_k^x = p_k^x \sqrt{\frac{4(p_k^t + \lambda(t_k - f(\tilde{x}_k))^2)}{C_p}}.$$

Taking the minimum of these two expressions for \tilde{p}_k^x , and calling this minimum $0 \leq m(N) \leq 1$ we have $\tilde{p}_k^x = m(N)p_k^x \leq p_k^x$ with $m(N) \rightarrow 1$ as $N \rightarrow \infty$. It also follows that

$$\frac{1}{N^{d+1}} \langle p_N, D_N v_N \rangle_N \leq m(N) E_N(v_N).$$

We now show the convergence of the liminf using the information we have just derived. First, since $v_N \xrightarrow{*} v$ holds by definition of weak*-convergence that

$$\int_{[0,1]^{d+1}} p \cdot Dv = \lim_{N \rightarrow \infty} \int_{[0,1]^{d+1}} p \cdot Dv_N = \lim_{N \rightarrow \infty} \frac{1}{N^{d+1}} \langle p_N, D_N v_N \rangle_N,$$

where the second inequality follows from Lemma 1. From the above argument, letting $N \rightarrow +\infty$ and then taking the supremum over p we get

$$E(v) \equiv \sup_{p \in K} \int_{[0,1]^{d+1}} p \cdot Dv \leq \liminf_{N \rightarrow \infty} E_N(v_N).$$

Note that the Neumann boundary conditions of the population problem are preserved in the finite sample version and consistency for those follows immediately by construction. This shows the first part of Γ -convergence.

Part (ii): For the second part we have to construct a recovering sequence (Dal Maso, 2012; Chambolle and Pock, 2021), which is a sequence v_N of discrete functions of the form

$$\tilde{v}_N(x) := \sum_{0 \leq k \leq N} \tilde{v}_k \mathbf{1}\{x \in Q_k\}$$

with $\tilde{v}_N \xrightarrow{*} v$ and

$$\limsup_{N \rightarrow \infty} E_N(\tilde{v}_N) \leq E(v).$$

By Ambrosio et al. (2000, Theorem 3.9) we can approximate $v \in BV([0,1]^{d+1})$ by a sequence $v_N \in C_c^\infty([0,1]^{d+1})$ of mollifiers in L^1 with

$$\lim_{N \rightarrow \infty} \int_{[0,1]^{d+1}} |\nabla v_N| \, dx = |Dv|.$$

We then construct the \tilde{v}_N by

$$\tilde{v}_N(x) = \sum_{0 \leq k \leq N} v_N(x_k) \mathbb{1}\{x \in Q_k\},$$

where x_k is the center point of the corresponding cube Q_k . But note that

$$\begin{aligned} & \lim_{N \rightarrow \infty} |\tilde{v}_N - v_N|_{L^1([0,1]^{d+1})} \\ &= \lim_{N \rightarrow \infty} \int_{[0,1]^{d+1}} \left| \sum_{0 \leq k \leq N} v_N(x_k) \mathbb{1}\{x \in Q_k\} - v(x) \right| dx \\ &\leq \lim_{N \rightarrow \infty} \int_{[0,1]^{d+1}} \left| \sum_{0 \leq k \leq N} v_N(x_k) \mathbb{1}\{x \in Q_k\} - v_N(x) \right| dx + o(1) \\ &= \lim_{N \rightarrow \infty} \int_{[0,1]^{d+1}} \left| \sum_{0 \leq k \leq N} v_N(x_k) \mathbb{1}\{x \in Q_k\} - \sum_{0 \leq k \leq N} v_N(x) \mathbb{1}\{x \in Q_k\} \right| dx + o(1) \\ &\leq \lim_{N \rightarrow \infty} \sum_{0 \leq k \leq N} \int_{Q_k} |v_N(x_k) - v_N(x)| dx + o(1) \\ &\leq \lim_{N \rightarrow \infty} \sum_{0 \leq k \leq N} \frac{L_N + o(1)}{2N} \frac{1}{N^{d+1}} + o(1) \\ &\leq \lim_{N \rightarrow \infty} \sum_{0 \leq k \leq N} \frac{L_N + o(1)}{2N^{d+2}} + o(1) \\ &\leq \lim_{N \rightarrow \infty} \frac{L_N + o(1)}{2N} + o(1) = 0, \end{aligned}$$

where we used the mean-value inequality and

$$L_N := \int_{[0,1]^{d+1}} |\nabla v_N| dx,$$

which we know converges to a bounded quantity since $v \in BV([0,1]^{d+1})$. This shows that $\tilde{v}_N \rightarrow v$ in $L^1([0,1]^{d+1})$.

Now we need to show that $\tilde{v}_N \xrightarrow{*} v$, for which we have to show that $\sup_{N \in \mathbb{N}} |D\tilde{v}_N| < +\infty$. Since $v_N \rightarrow v$ in $L^1([0,1]^{d+1})$, it holds that

$$|Dv_N| = \int_{[0,1]^{d+1}} |\nabla v_N| dx < +\infty$$

for N large enough (Ambrosio et al., 2000, Theorem 3.9). By construction, for any $N \in \mathbb{N}$

it holds that

$$\begin{aligned}
\int_{[0,1]^{d+1}} p \cdot D\tilde{v}_N &= \sum_{0 \leq k \leq N} \int_{Q_k} p \cdot D\tilde{v}_N \\
&= \sum_{0 \leq k \leq N} \int_{Q_k} p \cdot \nabla \tilde{v}_N + \sum_{0 \leq k \leq N} \int_{\partial Q_k^\uparrow \cap \partial Q_k} \left(\tilde{v}_k^\uparrow - \tilde{v}_k \right) p \cdot s \, d\mathcal{H}^d \\
&= \sum_{0 \leq k \leq N} \left(\tilde{v}_k^\uparrow - \tilde{v}_k \right) p^\uparrow \frac{1}{N^d} \\
&\leq \frac{1}{N^d} \sum_{0 \leq k \leq N} \frac{L}{N} p^\uparrow,
\end{aligned}$$

where p^\uparrow is the value of p on the boundary of one of the forward directions. Since p is continuous and $[0,1]^{d+1}$ is compact, it follows

$$\sup_{N \in \mathbb{N}} \sup_{p \in C_0([0,1]^{d+1})} \int_{[0,1]^{d+1}} p \cdot D\tilde{v}_N \leq \sup_{N \in \mathbb{N}} \sup_{p \in C_0([0,1]^{d+1})} \frac{1}{N^d} \sum_{0 \leq k \leq N} \frac{L}{N} p^\uparrow < +\infty,$$

which shows that $\sup_{N \in \mathbb{N}} |D\tilde{v}_N| < +\infty$. This in turn implies that $\tilde{v}_N \xrightarrow{*} v$, which shows that \tilde{v}_N is the required recovering sequence, since the Neumann boundary conditions are also preserved as before. \square

C.4 Proof of Theorem 2

Proof. The proof follows along similar lines to the proof of Proposition 2, except that we have to account for the randomness of the estimators $\hat{f}_{Nn}(\tilde{x}_k)$ and $\hat{f}_{X,h(n)}(\tilde{x}_k)$. The only random element in the optimization problem is one constraint in \hat{K} , and this is what we analyze. All the other arguments are the same as in the deterministic case and are omitted.

Recall that the constraint for \hat{K}_{Nn} reads

$$|p^x(x, t)|^2 \leq 4\hat{f}_{X,h(n)}(\tilde{x}_k) \left(p^t(x, t) + \lambda_n \hat{f}_{X,h(n)}(\tilde{x}_k) \left(t - \hat{f}_{Nn}(\tilde{x}_k) \right)^2 \right).$$

As before we analyze

$$|p_k^x|^2 \leq (|p_k^x - p^x(x_k)| + |p^x(x_k)|)^2,$$

where x_k is again the center point of the cube Q_k . The first term can be bounded in the same way as in Proposition 2:

$$|p_k^x - p^x(x_k)| \leq \frac{L}{2N}.$$

By the fact that $p \in K$ the second term satisfies

$$\begin{aligned}
|p^x(x_k)| &\leq 2\sqrt{\hat{f}_{X,h(n)}(\tilde{x}_k)p^t(x_k) + \lambda_n \hat{f}_{X,Nn}^2(\tilde{x}_k) \left(t_k - \hat{f}_{Nn}(\tilde{x}_k)\right)^2} \\
&\leq 2\sqrt{\hat{f}_{X,h(n)}(\tilde{x}_k) |p^t(x_k) - p_k^t| + \hat{f}_{X,h(n)}(\tilde{x}_k)p_k^t + \lambda_n \hat{f}_{X,Nn}^2(\tilde{x}_k) \left(t_k - \hat{f}_{Nn}(\tilde{x}_k)\right)^2} \\
&\leq 2\sqrt{\hat{f}_{X,h(n)}(\tilde{x}_k) \frac{L}{2N} + \hat{f}_{X,h(n)}(\tilde{x}_k)p_k^t + \lambda_n \hat{f}_{X,h(n)}^2(\tilde{x}_k) \left(t_k - \hat{f}_{Nn}(\tilde{x}_k)\right)^2},
\end{aligned}$$

where we define $x_k \equiv (\tilde{x}_k, t_k) \in \mathbb{R}^{d+1}$ and the second line follows from $(a - b) \leq |a - b|$. The difference to the deterministic case is that \hat{f}_{Nn} and $\hat{f}_{X,h(n)}$ are random estimators of $f(x)$ and $f_X(x)$, which in our discretization scheme are imputed in the center of each cube. Putting both terms together gives

$$|p_k^x|^2 \leq \left(\frac{L}{2N} + \sqrt{\hat{f}_{X,h(n)}(\tilde{x}_k) \frac{2L}{N} + \hat{f}_{X,h(n)}(\tilde{x}_k)p_k^t + \lambda_n \hat{f}_{X,Nn}^2(\tilde{x}_k) \left(t_k - \hat{f}_{Nn}(\tilde{x}_k)\right)^2} \right)^2.$$

Just as in the discrete case, we bound this further by

$$\begin{aligned}
(14) \quad |p_k^x|^2 &\leq \left(\frac{L}{2N} + \sqrt{\hat{f}_{X,h(n)}(\tilde{x}_k) \frac{2L}{N}} \right)^2 \\
&+ 2 \left(\frac{L}{2N} + \sqrt{\hat{f}_{X,h(n)}(\tilde{x}_k) \frac{2L}{N}} \right) \sqrt{4\hat{f}_{X,h(n)}(\tilde{x}_k) \left(p_k^t + \lambda_n \hat{f}_{X,h(n)}(\tilde{x}_k) \left(t_k - \hat{f}_{Nn}(\tilde{x}_k) \right)^2 \right)} \\
&\quad + 4\hat{f}_{X,h(n)}(\tilde{x}_k) \left(p_k^t + \lambda_n \hat{f}_{X,h(n)}(\tilde{x}_k) \left(t_k - \hat{f}_{Nn}(\tilde{x}_k) \right)^2 \right)
\end{aligned}$$

Addressing the randomness:

Let us consider the two terms $\hat{f}_{X,h(n)}(\tilde{x}_k)$ and $\hat{f}_{Nn}(\tilde{x}_k)$ one by one. First, by definition, $\hat{f}_{X,h(n)}(\tilde{x}_k)$ is a Nadaraya-Watson estimator. Corollary 3 in [Irle \(1997\)](#) in conjunction with Assumption 3 and the assumptions stated in Theorem 2 guarantees that $\hat{f}_{X,h(n)}(x)$ converges almost surely for almost every $x \in \mathbb{R}^d$ to $f_X(x)$. To see this, note that strict stationarity of $\{X_i\}$ implies asymptotic stationarity and in particular “summability” of the first two terms in the last equation on page 131 of [Irle \(1997\)](#). The last term of the summability condition of [Irle \(1997\)](#) follows since under Assumption 3 $s > 1$, which implies that there exists a small enough $k > 0$ such that $\sum_{i=1}^{\infty} \alpha(i)^{1/k} < +\infty$; in fact, we can set $0 < k < s$. The last assumption in Corollary 3 of [Irle \(1997\)](#) follows directly from Assumption 3. Then, by construction, \tilde{x}_k is a Lebesgue point, which implies that $\hat{f}_{X,h(n)}(\tilde{x}_k)$ converges almost surely to $f_X(\tilde{x}_k)$ since the latter is a density. The Continuous Mapping Theorem (e.g. [van der Vaart](#)

and Wellner, 1996, Theorem 1.3.6) implies that $\hat{f}_{X,h(n)}^2(\tilde{x}_k)$ also converges almost surely to $f_X^2(\tilde{x}_k)$.

Now write $Z_{ik} := 1\{i : X_i \in Q_k\}(f(X_i) + \varepsilon_i)$ with $S_k := \sum_{i=1}^n Z_{ik}$ for the numerator; and $I_{ik} := 1\{X_i \in Q_k\}$ with $M_k := \sum_{i=1}^n I_{ik}$. Then we can write

$$\hat{f}_{Nn}(\tilde{x}_k) = \frac{1}{\sum_{i=1}^n 1\{i : X_i \in Q_k\}} \sum_{i: X_i \in Q_k} (f(X_i) + \varepsilon_i) = \frac{S_k}{M_k}$$

Fix a cube Q_k and define the success probability of the Bernoulli random variable I_{ik} as $\pi_k = \int_{Q_k} f_X(x)dx$. By Assumption 3, $\pi_k \geq \frac{c_x}{N^d}$. By Theorem 3.49 in White (2014), the process $\{I_{ik}\}_i$ is α -mixing of the same size since $\{(X_i, \varepsilon_i)\}_i$ is α -mixing and I_{ik} is a measurable function of the process.

We want to bound $|\hat{f}_{Nn}(\tilde{x}_k) - \frac{\mathbb{E}[S_k]}{\mathbb{E}[M_k]}|$. We can write:

$$\left| \hat{f}_{Nn}(\tilde{x}_k) - \frac{\mathbb{E}[S_k]}{\mathbb{E}[M_k]} \right| = \left| \frac{S_k}{M_k} - \frac{\mathbb{E}[S_k]}{\mathbb{E}[M_k]} \right|.$$

Note that this is the correct relationship to bound since we want to compare the estimator to $\mathbb{E}[S_k | X_i \in Q_k] = \frac{\mathbb{E}[S_k]}{\mathbb{E}[M_k]}$. Now write

$$\begin{aligned} \left| \frac{S_k}{M_k} - \frac{\mathbb{E}[S_k]}{\mathbb{E}[M_k]} \right| &\leq \left| \frac{S_k}{M_k} - \frac{\mathbb{E}[S_k]}{M_k} \right| + \left| \frac{\mathbb{E}[S_k]}{M_k} - \frac{\mathbb{E}[S_k]}{\mathbb{E}[M_k]} \right| \\ &= \frac{1}{M_k} |S_k - \mathbb{E}[S_k]| + \mathbb{E}[S_k] \left| \frac{1}{M_k} - \frac{1}{\mathbb{E}[M_k]} \right|, \end{aligned}$$

and consider the first term first.

To bound the first term, consider the two events $\{\sum_i I_{ik} < \frac{nc_x}{2N^d}\}$ and $\{\sum_i I_{ik} \geq \frac{nc_x}{2N^d}\}$. The first one is the event that there are “not enough” data points in Q_k , the “bad event”.

We get:

$$\begin{aligned} P\left(\sum_{i=1}^n I_{ik} < \frac{nc_x}{2N^d}\right) &= P\left(\sum_{i=1}^n I_{ik} - \sum_{i=1}^n \mathbb{E}[I_{ik}] < \frac{nc_x}{2N^d} - \sum_{i=1}^n \mathbb{E}[I_{ik}]\right) \\ &\leq P\left(\sum_{i=1}^n I_{ik} - \sum_{i=1}^n \mathbb{E}[I_{ik}] < -\frac{nc_x}{2N^d}\right) \\ &\leq P\left(\left|\sum_{i=1}^n I_{ik} - \sum_{i=1}^n \mathbb{E}[I_{ik}]\right| > \frac{nc_x}{2N^d}\right) \\ &\leq 4 \exp\left(-\frac{c_x^2}{32}q\right) + 22\left(1 + \frac{8}{c_x}\right)^{1/2} q\alpha\left(\frac{n}{2N^d q}\right) =: A(n, N^d, q) \end{aligned}$$

for any integer $q \in [1, \frac{n}{2N^d}]$, where the second line follows from $p_k \geq \frac{c_x}{N^d}$ and every I_{ik} is a Bernoulli random variable; and the last line follows from a Hoeffding inequality for α -mixing processes (Bosq, 2012, Theorem 1.3). Above, we can set q to be any slowly changing function of $\frac{n}{N^d}$, like $\lfloor \sqrt{n} \rfloor$ or $\lfloor \log(n) \rfloor$, to trade-off the speed of convergence in both terms. Also, note that this will hold for any k since the smallest probability of landing in a cube is $c_x \frac{1}{N^d}$ by Assumption 3. Since we have bounded this “bad event”, we can now turn to the good event and condition on this.

We want to bound this with a similar concentration bound, but since ε_i do not need to have bounded support, we need the more general concentration bound (Bosq, 2012, Theorem 1.4). Since f is bounded on \mathcal{X} , $f(X_i)$ is bounded for all i ; in addition, ε_i possesses a moment generating function in a local neighborhood of zero by Assumption 3. Therefore $Y_i = f(X_i) + \varepsilon_i$ satisfies Cramér’s condition from Theorem 1.4 in Bosq (2012). For any $\delta > 0$, any $\frac{n}{N^d} \geq 2$, any integer $q \in [1, \frac{n}{2N^d}]$, and any each $k \geq 3$ we hence get:

$$\begin{aligned} & P\left(|S_k - \mathbb{E}[S_k]| > \delta \frac{nc_x}{2N^d}\right) \\ =: & P\left(|S_k - \mathbb{E}[S_k]| > \tilde{\delta} \frac{n}{N^d}\right) \\ \leq & a_1 \exp\left(-\frac{q\tilde{\delta}^2}{25m_2^2 + 5c\tilde{\delta}}\right) + a_2(k)\alpha\left(\left\lfloor \frac{n}{(q+1)N^d} \right\rfloor\right) =: B(n, N^d, q, \delta), \end{aligned}$$

where

$$\begin{aligned} a_1 &= 2\frac{n}{qN^d} + 2\left(1 + \frac{\tilde{\delta}^2}{25m_2^2 + 5c\tilde{\delta}}\right), \quad m_2^2 = \max_{1 \leq t \leq n} \mathbb{E}X_t^2, \\ a_2(k) &= 11\frac{n}{N^d} \left(1 + \frac{5m_k}{\tilde{\delta}}\right)^{\frac{2k}{2k+1}}, \quad m_k = \max_{1 \leq t \leq n} \|X_t\|_k. \end{aligned}$$

The same argument as above holds, i.e., we can pick an appropriate q that balanced the convergence of both terms, and hence proves convergence to zero of this event.

In order to put both bounds together and bound the entire first term, note that

$$\left\{ \frac{1}{M_k} |S_k - \mathbb{E}[S_k]| > \delta, M_k \geq \frac{n}{2N^d} \right\} \subset \left\{ |S_k - \mathbb{E}[S_k]| > \delta \frac{n}{2N^d} \right\},$$

so that

$$\begin{aligned} P\left(\frac{1}{M_k} |S_k - \mathbb{E}[S_k]| > \delta\right) &\leq P\left(M_k < \frac{n}{2N^d}\right) + P\left(|S_k - \mathbb{E}[S_k]| > \delta \frac{n}{2N^d}\right) \\ &\leq A(n, N^d, q_1) + B(n, N^d, q_2) \end{aligned}$$

for integers $q_1, q_2 \in [1, \frac{n}{2N^d}]$.

Now we need to bound the second term $\mathbb{E}[S_k] |M_k^{-1} - (\mathbb{E}[M_k])^{-1}|$. We approach this in the same way as the previous bound. First, notice that

$$|M_k^{-1} - (\mathbb{E}[M_k])^{-1}| \leq \left| \frac{M_k - \mathbb{E}[M_k]}{M_k \mathbb{E}[M_k]} \right|.$$

Now we split the problem into the “bad” event $\{M_k < \frac{n}{2N^d}\}$, which we can bound in the exact same way as above by $A(n, N^d, q)$, and the “good event” $\{M_k \geq \frac{n}{2N^d}\}$. For the good event, we have

$$\mathbb{E}[S_k] |M_k^{-1} - (\mathbb{E}[M_k])^{-1}| \leq \frac{\mathbb{E}[S_k]}{\mathbb{E}[M_k]} \frac{|M_k - \mathbb{E}[M_k]|}{M_k}.$$

Now note that

$$\mathbb{E}[S_k] = \sum_{i=1}^n \mathbb{E}[f(X_i) + \varepsilon_i | X_i \in Q_k] \cdot P(X_i \in Q_k) \leq \sum_{i=1}^n C \frac{1}{N^d} = C \frac{n}{N^d},$$

because $\mathbb{E}[\varepsilon_i | X_i] = 0$, the law of iterated expectations, and $f \leq C < +\infty$ by Assumption 3. Similarly, $\mathbb{E}[M_k] = \frac{n}{N^d}$, so that $\frac{\mathbb{E}[S_k]}{\mathbb{E}[M_k]} \leq C$.

Now focus on the good event and bound for any $\delta > 0$

$$\begin{aligned} & P \left(|M_k - \mathbb{E}[M_k]| > \frac{\delta}{2C} \cdot \frac{n}{N^d} \right) \\ & \leq 4 \exp \left(-\frac{\delta}{32C^2} q \right) + 22 \left(1 + \frac{8C}{\delta} \right)^{1/2} q \alpha \left(\frac{n}{2qN^d} \right) \\ & =: C(n, N^d, q) \end{aligned}$$

for any integer $q \in [1, \frac{n}{N^d}]$, using the bound established above for I_{ik} . Notice that

$$\left\{ \mathbb{E}[S_k] |M_k^{-1} - (\mathbb{E}[M_k])^{-1}| > \delta, M_k \geq \frac{n}{2N^d} \right\} \subset \left\{ |M_k - \mathbb{E}[M_k]| > \frac{\delta}{2C} \cdot \frac{n}{N^d} \right\}.$$

We can therefore bound the second term for $\delta > 0$

$$\begin{aligned} P \left(\mathbb{E}[S_k] |M_k^{-1} - (\mathbb{E}[M_k])^{-1}| > \delta \right) & \leq P \left(M_k < \frac{n}{2N^d} \right) + P \left(|M_k - \mathbb{E}[M_k]| > \frac{\delta}{2C} \cdot \frac{n}{N^d} \right) \\ & \leq A(n, N^d, q) + C(n, N^d, q). \end{aligned}$$

This implies that we can bound the entire expression as

$$P\left(\left|\hat{f}_{Nn}(\tilde{x}_k) - \frac{\mathbb{E}[S_k]}{\mathbb{E}[M_k]}\right| > \delta\right) \leq 2A(n, N^d, q) + B(n, N^d, q, \delta) + C(n, N^d, q, \delta).$$

This bound holds for every cube Q_k . To obtain a uniform bound over the entire grid, we take the union bound

$$P\left(\max_{1 \leq k \leq N^d} \left|\hat{f}_{Nn}(\tilde{x}_k) - \frac{\mathbb{E}[S_k]}{\mathbb{E}[M_k]}\right| > \delta\right) \leq N^d (2A(n, N^d, q) + B(n, N^d, q, \delta) + C(n, N^d, q, \delta)).$$

We want this expression to converge to zero. Analyze the terms $A(n, N^d, q)$ and $C(n, N^d, q, \delta)$ first. These terms depend on q and have two main terms: the first is exponential in q and the second takes the form $q \cdot \alpha(\frac{n}{2qN^d})$. We get to choose $q \in [1, \frac{n}{2N^d}]$. So pick $q = (\frac{n}{N^d})^\rho$ for some $0 < \rho < 1$. The exponential term is of the form $N^d \cdot \exp(-c(\frac{n}{N^d})^\rho)$ for some $0 < \rho < 1$ and some fixed constant c . Since $\frac{n}{N^d} \rightarrow +\infty$, the exponential term dominates and this term vanishes exponentially fast as $n \rightarrow +\infty$.

The term involving the α -mixing parameter is of the form $N^d \cdot (\frac{n}{N^d})^\rho \alpha(\frac{n}{2qN^d})$, where $\alpha(m) = O(m^{-s})$ by Assumption 3. We want the expression

$$T(n) = N^d \cdot \left(\frac{n}{N^d}\right)^\rho \cdot \alpha\left(\frac{n^{1-\rho}}{2N^{d(1-\rho)}}\right) \leq N^d \cdot \left(\frac{n}{N^d}\right)^\rho \cdot C \cdot \left(\frac{n^{1-\rho}}{2N^{d(1-\rho)}}\right)^{-s}$$

to be bounded above by n^{-r} for some $r > 0$, in order to show almost sure convergence over all bins by a Borel-Cantelli-argument further down. We do this by picking an appropriate $\rho \in (0, 1)$. Some calculations show that if

$$\rho \leq \frac{s - m(1 + s) - r}{(1 + s)(1 - m)}$$

then $T(n) = O(n^{-r})$ for some fixed constant for all n . Also note that this $\rho \in (0, 1)$ because $s > \max\left\{\frac{r+m}{1-m}, \frac{r+1}{2k+1(1-m)}\right\}$ by Assumption 3.

Now turn to analyzing $B(n, N^d, q, \delta)$, which is again split into an exponential term and the α -mixing term. For $q = (\frac{n}{N^d})^\rho$ for $\rho \in (0, 1)$, the exponential term dominates, so focus again on the α -mixing term. We have to analyze $a_2(k)\alpha\left(\left\lfloor \frac{n}{(q1)N^d} \right\rfloor\right)$ in Theorem 1.4 of Bosq (2012). To simplify, we assume that $\frac{n}{(q1)N^d}$ is an integer without loss of generality. We want to guarantee that $N^d \frac{n}{N^d} \left(\frac{n}{((\frac{n}{N^d})^\rho + 1)N^d}\right)^{-s}$ is bounded above by n^{-r} for some $r > 1$. Some

more calculations show that if

$$\rho \leq \frac{s \frac{2k}{2k+1} (1-m) - r - 1}{s \frac{2k}{2k+1} (1-m)},$$

then $T(n) = O(n^{-r})$ for some fixed constant $C < +\infty$ over all n . Again, since $s > \max \left\{ \frac{r+m}{1-m}, \frac{r+1}{\frac{2k}{2k+1}(1-m)} \right\}$ by Assumption 3, $\rho \in (0, 1)$.

Hence picking

$$\rho \leq \min \left\{ \frac{s - m(1+s) - r}{(1+s)(1-m)}, \frac{s \frac{2k}{2k+1} (1-m) - r - 1}{s \frac{2k}{2k+1} (1-m)} \right\}$$

ensures that

$$P \left(\max_{1 \leq k \leq N^d} \left| \hat{f}_{Nn}(\tilde{x}_k) - \frac{\mathbb{E}[S_k]}{\mathbb{E}[M_k]} \right| > \delta \right) \leq Cn^{-r}$$

for some constant $C < +\infty$.

We now show the almost sure convergence uniformly over all cubes Q_k . For each $n \in \mathbb{N}$, consider the event

$$A_n := \left\{ \max_{1 \leq k \leq N^d} \left| \hat{f}_{Nn}(\tilde{x}_k) - \frac{\mathbb{E}[S_k]}{\mathbb{E}[M_k]} \right| > \delta \right\},$$

and the above computations show that $P(A_n) \leq Cn^{-r}$. Hence,

$$\sum_{i=1}^n P(A_n) \leq C \sum_{i=1}^n n^{-r} < +\infty$$

and the Borel-Cantelli Lemma implies that A_n occurs infinitely often with probability zero. Thus, for large enough n , almost surely $A_n = 0$, which shows the almost sure convergence of $\hat{f}_{nN}(\tilde{x}_k)$ to $\lim_{N \rightarrow +\infty} \frac{\mathbb{E}[S_k]}{\mathbb{E}[M_k]}$.

If f is continuous at \tilde{x}_k , then, focusing on a sequence of cubes $\{Q_k\}_N$ shrinking in such a way that they all contain \tilde{x}_k , the classical Lebesgue-Besicovitch differentiation theorem (e.g. [Evans and Gariepy, 2018](#), section 1.7.1) implies that $\hat{f}_{Nn}(\tilde{x}_k) = \lim_{N \rightarrow +\infty} \frac{\mathbb{E}[S_k]}{\mathbb{E}[M_k]} = \frac{f(\tilde{x}_k)f_X(\tilde{x}_k)}{f_X(\tilde{x}_k)} = f(\tilde{x}_k)$.

If $\tilde{x}_k \in S_f$ the limit value depends on how the cubes shrink while containing x_k . We can write

$$\begin{aligned} \lim_{N \rightarrow +\infty} \hat{f}_{Nn}(\tilde{x}_k) &= \lim_{N \rightarrow +\infty} \frac{\int_{Q_{kN}} f(x) f_X(x) dx}{\int_{Q_{kN}} f_X(x) dx} \\ &= \lim_{N \rightarrow +\infty} \frac{\int_{Q_{kN} \cap H^+(\tilde{x}_k, \rho)} f(x) f_X(x) dx + \int_{Q_{kN} \cap H^-(\tilde{x}_k, \rho)} f(x) f_X(x) dx}{\int_{Q_{kN}} f_X(x) dx}, \end{aligned}$$

where Q_{kN} is a sequence of cubes containing \tilde{x}_k such that they converge to $\{\tilde{x}_k\}$ and $H^+(\tilde{x}_k, \rho) = \{y : \langle y - x, \rho \rangle \geq 0\}$ and $H^-(\tilde{x}_k, \rho) = \mathbb{R}^d \setminus H^+(\tilde{x}_k, \rho)$ are the two half spaces created by the Hyperplane $H(\tilde{x}_k, \rho)$ oriented by some $\rho \in S^{d-1}$ in the direction of the jump of f at \tilde{x}_k , as depicted in Figure A-1. Since each Q_{kN} intersects both half balls for all N , the limit $\lim_{N \rightarrow +\infty} \hat{f}_{Nn}(\tilde{x}_k)$ converges by the Lebesgue-Besicovitch differentiation theorem to the convex combination

$$\lim_{N \rightarrow +\infty} \hat{f}_{Nn}(\tilde{x}_k) = (1 - \theta)f^+(\tilde{x}_k) + \theta f^-(\tilde{x}_k),$$

where

$$0 < \theta = \lim_{N \rightarrow +\infty} \frac{\int_{Q_{kn} \cap H^+(\tilde{x}_k, \rho)} f_X(x) dx}{\int_{Q_{kn}} f_X(x) dx} < 1.$$

Note that since cubes are symmetric with respect to their center point, any hyperplane going through the center point of Q_k and dissecting it splits Q_k into two subsets of the same Lebesgue measure. Hence if f_x is the density of the continuous uniform distribution and the grid consists of all cubes, then $\theta = 1/2$.

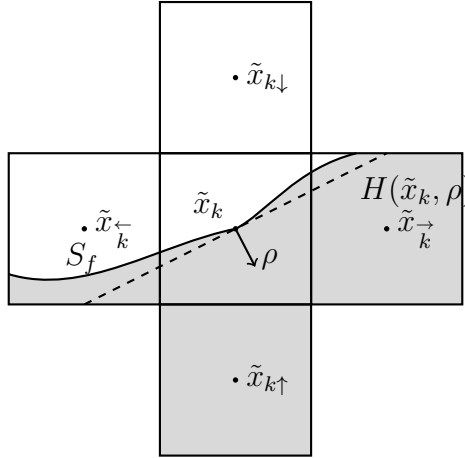


Figure A-1: Representation of the case $\tilde{x}_k \in S_f$.

Putting everything together:

The argument is essentially the same as in the proof of Proposition 2, except that we allow for $\lambda_n \rightarrow +\infty$ and the bounds are now

$$\tilde{p}_k^x = p_k^x \left(\frac{\nu}{\nu + o(1) + \frac{L}{2N}} \right) \quad \text{and} \quad \tilde{p}_k^x = p_k^x \sqrt{\frac{S^2}{R^2 + 2RS + S^2}},$$

with

$$R := \frac{L}{2N} + \sqrt{\hat{f}_{X,h(n)}(\tilde{x}_k) \frac{2L}{N}}, \quad S := \sqrt{4\hat{f}_{X,h(n)}(\tilde{x}_k) \left(p_k^t + \lambda_n \hat{f}_{X,h(n)}(\tilde{x}_k) \left(t_k - \hat{f}_{Nn}(\tilde{x}_k) \right)^2 \right)}.$$

Taking the minimum of these two expressions for \tilde{p}_k^x , and calling this minimum $0 \leq m(N) \leq 1$ we first want to show that $m(N)$ converges almost surely to 1 as $N(n) \rightarrow +\infty$. Since $\hat{f}_{X,h(n)} \xrightarrow{a.s.} f_X$ as $n \rightarrow +\infty$, where f_X is bounded above by Assumption 3, $R^2 \rightarrow 0$ almost surely. Now analyze $2RS$:

$$\begin{aligned} RS &= \left(\frac{L}{2N} + \sqrt{\hat{f}_{X,h(n)}(\tilde{x}_k) \frac{2L}{N}} \right) \sqrt{4\hat{f}_{X,h(n)}(\tilde{x}_k) \left(p_k^t + \lambda_n \hat{f}_{X,h(n)}(\tilde{x}_k) \left(t_k - \hat{f}_{Nn}(\tilde{x}_k) \right)^2 \right)} \\ &= \sqrt{\frac{L^2}{N^2} \hat{f}_{X,h(n)}(\tilde{x}_k) \left(p_k^t + \lambda_n \hat{f}_{X,h(n)}(\tilde{x}_k) \left(t_k - \hat{f}_{Nn}(\tilde{x}_k) \right)^2 \right)} \\ &\quad + \sqrt{\frac{8L}{N} \hat{f}_{X,h(n)}^2(\tilde{x}_k) \left(p_k^t + \lambda_n \hat{f}_{X,h(n)}(\tilde{x}_k) \left(t_k - \hat{f}_{Nn}(\tilde{x}_k) \right)^2 \right)}. \end{aligned}$$

Since f_X and \tilde{f} are bounded and both $\hat{f}_{X,h(n)}$ and \hat{f}_{Nn} are almost surely consistent for f_X and \tilde{f} , it follows from $\lambda_n = o(N)$ that the both terms converge to 0 almost surely, which implies that $RS \rightarrow 0$ almost surely. This shows that $m(N) \rightarrow 1$ almost surely. The rest of the argument now is the same as in Proposition 2. \square

Appendix D Implementation

We solve (4) using a primal-dual algorithm (Chambolle and Pock, 2011). At each step, we need to project the iterand v^n , which denotes the estimated primal function v at the n -th iteration of the algorithm, onto the sets C and K . We now discuss how these projections are implemented, before presenting the algorithm. The implementation follows those of Strekalovskiy et al. (2012) and Bauer (2016).

D.1 Projection Onto Constraint Sets

Projection Onto C The projection onto C can be done using a straightforward clipping,

$$(15) \quad v^{n+1} = \min\{1, \max\{0, v^n\}\},$$

where v^n is the n -th iteration of the discretized function v . We also need to impose the discretized limits from C , by setting $v^{n+1}(k_1, \dots, k_d, 1) = 1$ and $v^{n+1}(k_1, \dots, k_d, N) = 0$.

Projection Onto K The projection onto K is more involved. The first constraint,

$$(16) \quad K_1 = \left\{ p^t(k) \geq \frac{|p^x(k)|_2^2}{4} - \lambda \left(\frac{k}{S} - f(k_1, \dots, k_d) \right)^2 \right\},$$

constitutes a pointwise projection onto a parabola, which can be rewritten as an optimization program. To see this, let $\alpha > 0, p^x \in \mathbb{R}^d, p^t \in \mathbb{R}$ and $p = (p^x, p^t)^T \in \mathbb{R}^d \times \mathbb{R}$. Assume that $p_0^t < \alpha |p_0^x|_2^2$ holds for a point $p_0 \in \mathbb{R}^d \times \mathbb{R}$. The projection of p_0 onto the parabola $\alpha |p^x|_2^2$ can then be written as the following optimization program:

$$\begin{aligned} \min_{p \in \mathbb{R}^d \times \mathbb{R}} \quad & \frac{1}{2} |p - p_0|_2^2 \\ \text{subject to} \quad & p^t \geq \alpha |p^x|_2^2, \end{aligned}$$

where $\alpha = \frac{1}{4\hat{f}_{X,N_n}(k_1, \dots, k_d)}$ and we leave out the constant $\lambda \hat{f}_{X,N_n}(\dots) \left(\frac{k}{N} - f(\dots) \right)^2$ for ease of notation. The first-order conditions of the corresponding Lagrangian are,

$$(17) \quad \begin{pmatrix} p^x - p_0^x + \mu 2\alpha p^x \\ p^t - p_0^t - \mu \\ \alpha |p^x|_2^2 - p^t \end{pmatrix} = 0.$$

Solving for μ and recombining gives the cubic equation,

$$t^3 + 3bt - 2a = 0$$

with $a = 2\alpha |p_0^x|_2^2, b = \frac{2}{3} (1 - 2\alpha p_0^t)$ and $t = 2\alpha |p^x|_2^2$, which can be solved analytically as (McKelvey, 1984),

$$p^x = \begin{cases} p_0^x & \text{if } p_0^t \geq \alpha |p_0^x|_2^2 \\ \frac{w}{2\alpha} \frac{p_0^x}{|p_0^x|_2^2} & \text{if } p_0^t < \alpha |p_0^x|_2^2 \text{ and } p_0^x \neq 0 \\ 0 & \text{else} \end{cases}$$

and

$$p^t = \begin{cases} p_0^t & \text{if } p_0^t \geq \alpha |p_0^x|_2^2 \\ \alpha |p^x|_2^2 & \text{else} \end{cases},$$

where

$$d = \begin{cases} a^2 + b^3 & \text{if } b \geq 0 \\ \left(a - \sqrt{-b^3}\right) \left(a + \sqrt{-b^3}\right) & \text{else} \end{cases}$$

and

$$w = \begin{cases} 0 & \text{if } c = 0 \\ c - \frac{b}{c} & \text{if } d \geq 0 \text{ and } c > 0, \\ 2\sqrt{-b} \cos\left(\frac{1}{3} \arccos \frac{a}{\sqrt{-b^3}}\right) & \text{else} \end{cases}$$

with $c = \sqrt[3]{a + \sqrt{d}}$.

The second constraint, we decouple from the first by way of Lagrange multipliers (Strekalovskiy et al., 2012). This lets us avoid the Dykstra projection originally used in Pock et al. (2009), which requires nested iterations (outer loop: primal-dual algorithm, inner loop: Dykstra's algorithm) and is thus computationally costly. In particular, we introduce a set of auxiliary variables $s_{s_1, s_2} := \sum_{s_1 \leq k_{d+1} \leq s_2} p^x(k)$ and of Lagrange multipliers $\mu_{s_1, s_2} \in \mathbb{R}^d$ and write the second constraint set as,

$$(18) \quad K_2 = \left\{ |s_{s_1, s_2}| \leq \nu \text{ s.t. } s_{s_1, s_2} = \sum_{s_1 \leq k_{d+1} \leq s_2} p^x(k) \right\},$$

with corresponding Lagrangian,

$$(19) \quad \mathcal{L}(v, \mu, p, s) = \langle p, D_N v \rangle_N + \sum_{s_1=1}^S \sum_{s_2=k_1}^S \left\langle \mu_{s_1, s_2}, \sum_{s_1 \leq k_{d+1} \leq s_2} p^x(k) - s_{s_1, s_2} \right\rangle.$$

Then, let (v^*, p^*) be the solution to (4) and $(v^*, p^*, \mu_{s_1, s_2}^*, s_{s_1, s_2}^*)$ the solution to,

$$(20) \quad \min_{v \in C} \max_{\substack{p \in K_1 \\ \mu_{s_1, s_2} \mid |s_{s_1, s_2}| \leq \nu}} \mathcal{L}(v, \mu, p, s).$$

We have that,

$$(21) \quad \langle p^*, D_N v^* \rangle_N = \mathcal{L}(v^*, \mu^*, p^*, s^*),$$

because $p \in K$ implies $p \in K_2$ and hence the Lagrange constraint $s_{s_1, s_2} = \sum_{s_1 \leq k_{d+1} \leq s_2} p^x(k)$ always holds with equality at the optimum.

D.2 Algorithm

Putting everything together, we solve the discretized problem using a primal-dual gradient descent-ascent algorithm (Chambolle and Pock, 2011). To calculate the gradient updates, we just need the derivatives with respect to the Lagrangian above, which are,

$$(22) \quad \begin{aligned} \frac{\partial \mathcal{L}(u, \mu, p, s)}{\partial u} &= D_N^T p \\ \frac{\partial \mathcal{L}(u, \mu, p, s)}{\partial s_{s_1, s_2}} &= -\mu_{s_1, s_2} \\ \frac{\partial \mathcal{L}(u, \mu, p, s)}{\partial \mu_{s_1, s_2}} &= p^x(k) - s_{s_1, s_2} \\ \frac{\partial \mathcal{L}(u, \mu, p, s)}{\partial p} &= D_N u + \tilde{p}, \end{aligned}$$

where

$$(23) \quad \tilde{p} = \begin{pmatrix} \sum_{s_1=1}^l \sum_{s_2=l}^S \mu_{s_1, s_2}^1 \\ \sum_{s_1=1}^l \sum_{s_2=l}^S \mu_{s_1, s_2}^2 \\ 0 \end{pmatrix}.$$

We get the following algorithm, It was proved in Chambolle and Pock (2011, Thm.1) that

Algorithm 1 Primal-Dual Algorithm

- 1: Choose $(v^0, p^0, \mu^0, s^0) \in C \times K_p \times \mathbb{R}^{d \times N_1 \times \dots \times N_d \times I} \times \mathbb{R}^{d \times N_1 \times \dots \times N_d \times I}$ and let $\bar{v}^0 = u^0, \bar{\mu}^0 = \mu^0 = 0, p^0 = 0$.
- 2: Set $\tau_v = \sigma_p = \frac{1}{4(d+1)}$ and $\tau_\mu = 1/I, \sigma_s = 1$.
- 3: For each $n \geq 0$:
- 4:

$$\left\{ \begin{aligned} p^{n+1} &= \Pi_{K_p} (p^n + \sigma_p (D_N \bar{v}^n + \tilde{p}^n)) \\ s_{s_1, s_2}^{n+1} &= \Pi_{|\cdot| \leq \nu} (s_{s_1, s_2}^n - \sigma_s \bar{\mu}_{s_1, s_2}^n) \\ v^{n+1} &= \Pi_C (v^n - \tau_v D_N^* p^{n+1}) \\ \mu_{s_1, s_2}^{n+1} &= \mu_{s_1, s_2}^n + \tau_\mu \left(s_{s_1, s_2}^{n+1} - \sum_{s_1 \leq k_{d+1} \leq s_2} p^{x, n+1}(k) \right) \\ \bar{v}^{n+1} &= 2v^{n+1} - v^n \\ \bar{\mu}_{s_1, s_2}^{n+1} &= 2\mu_{s_1, s_2}^{n+1} - \mu_{s_1, s_2}^n, \end{aligned} \right.$$

where $\Pi_D(x)$ denotes the projection of x onto the set D , $I := \frac{S^2+S}{2}$ the number of K constraints, and $D_N^* = D_N^T := N \cdot D^T := -N \cdot \text{div}$ the adjoint of the discrete gradient operator.^a

- 5: **return** v^*

^aImplemented in practice as backward differences with a Neumann boundary condition.

$v \rightarrow v^*$ for this algorithm as the number of iterations n goes to infinity, under the condition that the step sizes satisfy $\tau\sigma L^2 < 1$, where $L = |K| := \max\{|Kx| : x \in X \text{ with } |x| \leq 1\}$ with K the continuous linear operator on the primal variable.

D.3 Computational Details and Code

We implement the described algorithm in [PyTorch](#), a modern deep learning framework that offers native support for GPU acceleration. Running the algorithm on a GPU, as opposed to a CPU, provides several advantages. GPUs are inherently designed for high-throughput parallelism, enabling the simultaneous processing of thousands of matrix operations. PyTorch offers native support for the whole spectrum of GPU architectures, including NVIDIA, Apple Silicon (for late 2020 Apple computers onward), and Intel GPUs. This ensures that researchers and practitioners with varied hardware setups can readily apply the estimator. For efficient computation of the SURE, which requires solving the algorithm a large number of times, we rely on the hyperparameter tuning suite in [Ray](#), an open-source distributed computing framework that supports parallel and fractional GPU processing. This can drastically speed up the hyperparameter selection by efficiently allocating jobs across multiple partitions of a single GPU on a local machine or multiple GPUs on a high-performance computing cluster.

The accompanying Python library can be found at <https://github.com/Davidvandijcke/fdr>. A fully developed Python package as well as extensions to R and STATA are in progress. Though the package is compatible with all major GPU architectures, researchers without GPUs on their local machines can refer to our Google Colab notebooks, which provide free access to cloud-based machines with GPU support. The current implementation of the algorithm takes 69.37 seconds on a Nvidia Tesla A100 Tensor Core GPU to converge on a 2D dataset with the number of raw data points $n = 90,000$, the number of grid points $N = 12,750$ (25%), and the discretization of the lifted dimension $S = 32$. This computation time can be further improved by approximating the objective function using “sublabel-accurate” relaxations ([Mollenhoff and Cremers, 2017](#)). As this requires further extensions of our statistical convergence arguments, we leave this to future work.

Appendix E Uncertainty Quantification

E.1 Subsampling

We construct uniform confidence bands by way of a subsampling approach with an estimated rate of convergence ([Politis et al., 1999](#), Ch.8). The only assumption required for

Algorithm 2 Subsampling

- 1: **Input:** Data $(X_i, Y_i), \mathcal{I} := \{1, \dots, n\}$, miscoverage level $\alpha \in (0, 1)$, regression algorithm \mathcal{A}
 - 2: **Output:** Confidence band, over $x \in \mathcal{Q}_{N_-}$
 - 3: $\hat{u} = \mathcal{A}(\{(X_i, Y_i) : i \in \mathcal{I}\})$
 - 4: **for** $j = 1$ to J **do**
 - 5: Randomly sample \mathcal{I} into K subsets $\mathcal{I}_1, \dots, \mathcal{I}_K$ of size b_1, \dots, b_K
 - 6: $u_{j,k}^* := \mathcal{A}(\{(Y_i, X_i) : i \in \mathcal{I}_k\})$
 - 7: $Z[j, k] = \max\{|u_{j,k}^* - \hat{u}|\}$
 - 8: **end for**
 - 9: $\bar{y}_k := \frac{1}{L} \sum_{\ell=1}^L \log [G_{b_k}^{*-1}(t_\ell) - G_{b_k}^{*-1}(s_\ell)]$, the mean of L log differences of the empirical quantile functions $G_b^{*-1}(t)$ at quantiles s_ℓ, t_ℓ
 - 10: $\hat{\beta} := -\frac{\text{cov}\{\bar{y}_k, \log(b_k)\}}{\text{var}\{\log(b_k)\}}$ the rate of convergence
 - 11: For some $k \in 1, \dots, K$:
 - 12: $Z^* = b_k^{\hat{\beta}} \cdot \max\{|\mathbf{u}_k^* - \hat{u}|\}$ with $\mathbf{u}_k^* = (u_{1,k}^*, \dots, u_{J,k}^*)$
 - 13: $z_\alpha := \text{sort}(Z^*)[(J+1) \cdot (\alpha)]$ the critical value
 - 14: **return** $C_{\text{sub}}(x, \alpha) = [\hat{u}(x) - z_\alpha/n^{b_k}, \hat{u}(x) + z_\alpha/n^{b_k}]$, for all $x \in \mathcal{Q}_{N_-}$
-

this approach to be consistent is that the limiting distribution exists and is non-degenerate for the rate of convergence we estimate. Under this assumption, we construct uniform confidence bounds using Algorithm 2, where \mathcal{Q}_{N_-} is the grid on the domain only, that is, without the lifted dimension. Note that, since we aim to construct confidence bands around a non-parametric estimate \hat{u} on a grid of size N , we keep the grid size fixed when calculating the subsampled estimates $u_{j,k}^*$. With this algorithm, we obtain the confidence bands and 95% significant jump sets depicted in Figures 1 and 3. To obtain confidence bands on the jump sizes, we simply repeat lines 8–14 in Algorithm 2 for the forward difference of \hat{u} and of the subsampled u^* s and conclude that a jump at point $x \in S_u$ is significant at the $\alpha\%$ level if either $\max\{y : y \in C_{\text{sub, lower}}^D(x, \alpha)\} > 0$, or $\min\{y : y \in C_{\text{sub, upper}}^D(x, \alpha)\} < 0$, where C^D indicates the confidence bands for the forward differences and “lower”, “upper” indicate whether we consider the upper or lower bound. We take the max and min since in practice we set the jump size equal to the largest forward difference along any of the axes.

E.2 Conformal Inference

As a computationally efficient, though more conservative, alternative to quantifying the uncertainty of the function \hat{u} and the jump set S_u , we rely on distribution-free conformal prediction methods developed for the non-parametric regression setting (Lei et al., 2018). Conformal prediction, originally, is a method for constructing bands around predictions produced by machine learning methods. Its appeal lies in the fact that it can produce prediction

bands for any general estimator without requiring assumptions about its properties or about the distribution of the data-generating process. In particular, we construct confidence bands around u and $|\nabla u|$ using the Split Conformal Prediction Algorithm 3 proposed in [Lei et al. \(2018, Algorithm 2\)](#). The authors show that, for $(X_i, Y_i)_{i=1, \dots, n}$ i.i.d. and assuming that the

Algorithm 3 Split Conformal Prediction ([Lei et al., 2018](#))

- 1: **Input:** Data $(X_i, Y_i), i = 1, \dots, n$, miscoverage level $\alpha \in (0, 1)$, regression algorithm \mathcal{A}
 - 2: **Output:** Prediction band, over $x \in \mathbb{R}^d$
 - 3: Randomly split $\{1, \dots, n\}$ into two equal-sized subsets $\mathcal{I}_1, \mathcal{I}_2$
 - 4: $\hat{\mu} = \mathcal{A}(\{(X_i, Y_i) : i \in \mathcal{I}_1\})$
 - 5: $R_i = |Y_i - \hat{\mu}(X_i)|, i \in \mathcal{I}_2$
 - 6: $d(\alpha)$ = the k th smallest value in $\{R_i : i \in \mathcal{I}_2\}$, where $k = \lceil (n/2 + 1)(1 - \alpha) \rceil$
 - 7: **return** $C_{\text{split}}(x, \alpha) = [\hat{\mu}(x) - d(\alpha), \hat{\mu}(x) + d(\alpha)]$, for all $x \in \mathbb{R}^d$
-

residuals $R_i, i \in \mathcal{I}_2$ have a continuous joint distribution, which is guaranteed in the limit under the Gaussian assumption for the SURE,

$$\mathbb{P}(Y_{n+1} \in C_{\text{split}}(X_{n+1}, \alpha)) \leq 1 - \alpha + \frac{2}{n+2}.$$

Thus, C_{split} delivers prediction bands for every grid point $x \in \mathcal{Q}_{N-}$ on which we estimate $\hat{u}(x)$.

In practice, we adapt Algorithm 3 to our grid-based setting as follows. Keeping the hyperparameters λ, ν and the grid \mathcal{Q}_N fixed, randomly split $\{1, \dots, n\}$ into equal subsets $\mathcal{I}_1, \mathcal{I}_2$ and cast $(X_i, Y_i), i \in \mathcal{I}_1$ onto \mathcal{Q}_N as in Section 3.2. Solve problem (4) on the grid, and then calculate R_i as the difference between Y_i and the prediction $\hat{u}(X'_i)$ for the grid point $X'_i \in \mathcal{Q}_{N-}$ closest to X_i . This gives prediction bands for the outcome variable Y_i . To obtain prediction bands for the jump set J_f , we also calculate the residual vector R_i^J for the implied predictions $D\hat{u}$ by computing DY'_i where Y'_i is the outcome value corresponding to the data point X_i closest to the grid point X'_i . Inference on the jump set then proceeds identically to the subsampling case. Finally, we stress that these *prediction* bands allow us to do inference on Y , but not on the conditional mean $f(X)$. Confidence bands for the latter will always be smaller than prediction bands for the former, so this approach provides a computationally efficient but very conservative hypothesis test regarding $f(X)$ and the corresponding jump set J_f . If the goal is to do inference on $f(X)$, we recommend using the subsampling approach described in the previous section.

Appendix F Additional Results

F.1 Figures

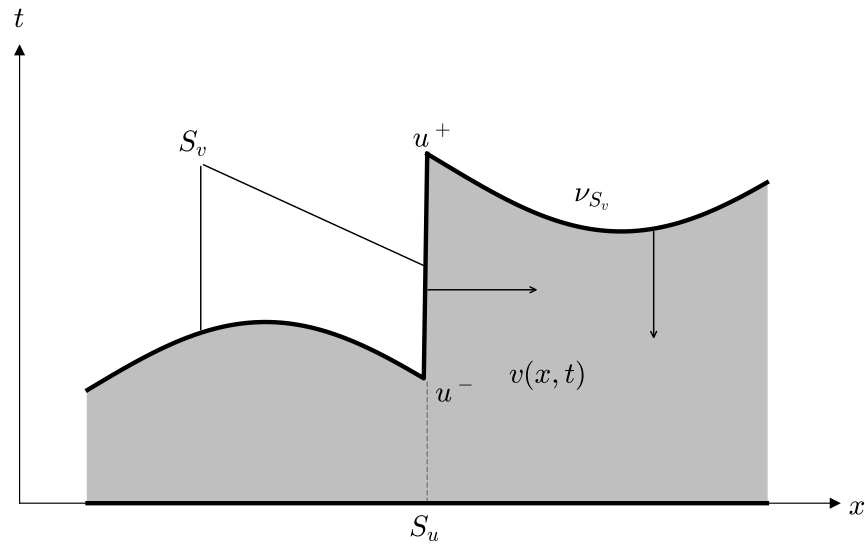


Figure A-2: Convex Relaxation Through Functional Lifting

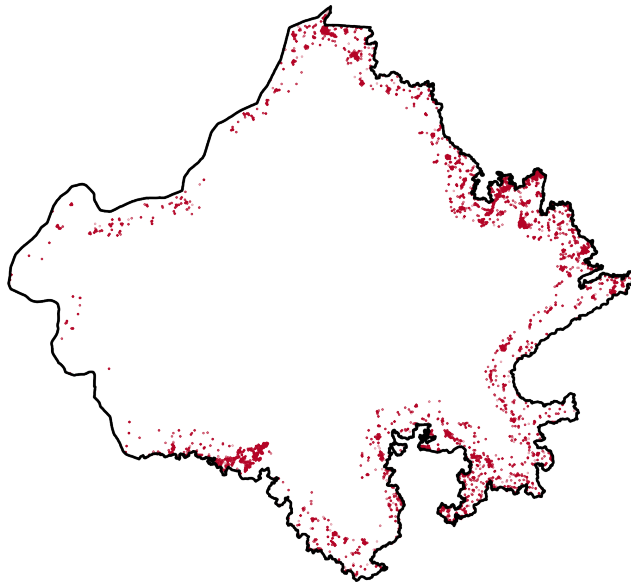
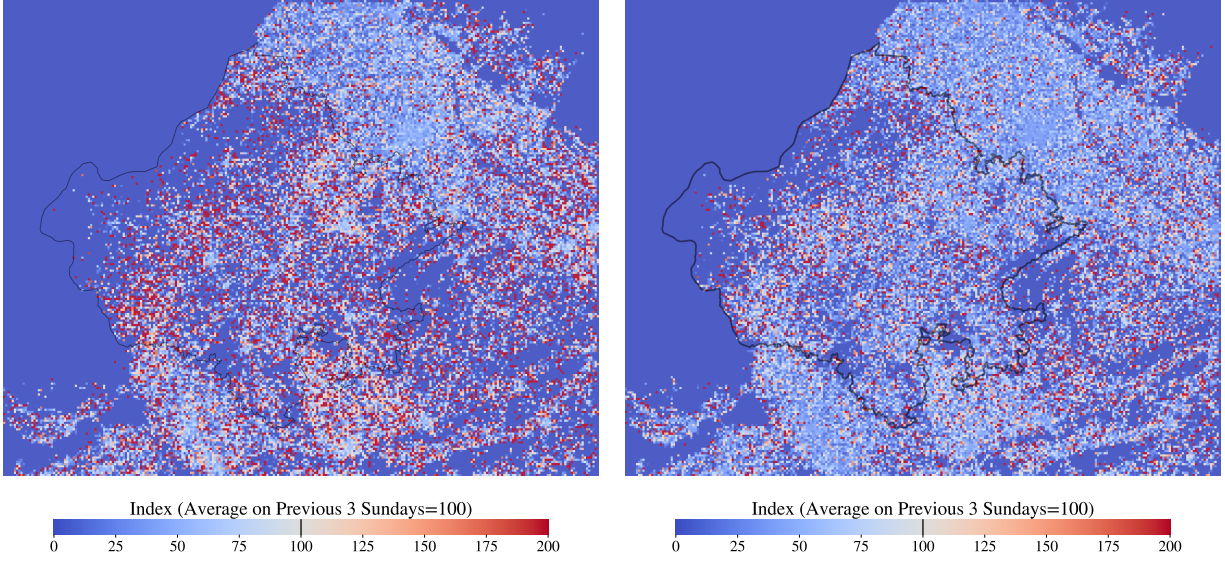


Figure A-3: Catchment Area for Estimating Degree of Selection

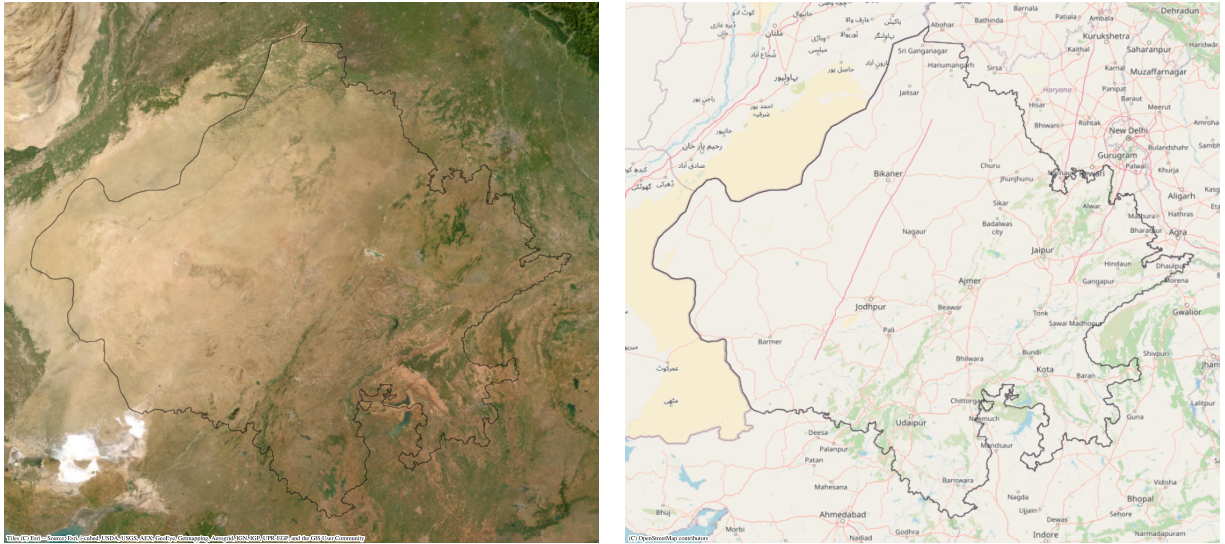
Note: Figure plots pings inside 40km band within Rajasthan around the state boundary during the shutdown period. The degree of self-selection is estimated by comparing the share of devices associated with these pings that cross into neighboring states with its average in the prior month.



(a) Mobile: Raw Data, Day Of, 6 pm – Midnight (b) Mobile: Raw Data, Day After, 6 am – 6 pm

Figure A-4: Post-Shutdown Activity

Note: Plot shows the raw mobile device data on a 5x5km grid with the fill color of each cell indicating the value of \bar{P}_{ings} , for the hours between 6 pm and midnight on the day of the shutdown in (a) and for the time spanning the shutdown window the day after the shutdown in (b). The outline of Rajasthan state is indicated by black lines.



(a) Esri Satellite Imagery

(b) OpenStreetMap

Figure A-5: Rajasthan: Terrain View

Note: A-5a shows the satellite view of Rajasthan, obtained from Esri; A-5b shows the street map of Rajasthan obtained from OpenStreetMap. The outline of Rajasthan is depicted in black.

References

- Abdulkadiroğlu, A., Angrist, J. D., Narita, Y., and Pathak, P. (2022). Breaking ties: Regression discontinuity design meets market design. *Econometrica*, 90(1):117–151.
- Alberti, G., Bouchitté, G., and Dal Maso, G. (2003). The calibration method for the Mumford–Shah functional and free-discontinuity problems. *Calculus of Variations and Partial Differential Equations*, 16(3):299–333.
- Alberti, G., Bouchitté, G., and Maso, G. D. (2001). The calibration method for the Mumford–Shah functional and free-discontinuity problems. *arXiv math/0105013*.
- Aliprantis, C. D. and Border, K. C. (2006). *Infinite dimensional analysis—A hitchhiker’s guide*. Springer.
- Ambrosio, L., Fusco, N., and Pallara, D. (2000). *Functions of bounded variation and free discontinuity problems*. Oxford University Press.
- Andrews, D. W. (1993). Tests for parameter instability and structural change with unknown change point. *Econometrica: Journal of the Econometric Society*, pages 821–856.
- Android Authority (2022). We asked, you told us: Most of you keep location tracking enabled. <https://tinyurl.com/55f5mp2s>.
- Argyle, B. S., Nadauld, T. D., and Palmer, C. J. (2020). Monthly payment targeting and the demand for maturity. *The Review of Financial Studies*, 33(11):5416–5462.
- Aue, A., Hörmann, S., Horváth, L., and Reimherr, M. (2009). Break detection in the covariance structure of multivariate time series models. *Annals of Statistics*.
- Bai, J. and Perron, P. (2003). Computation and analysis of multiple structural change models. *Journal of applied econometrics*, 18(1):1–22.
- Bauer, M. (2016). *Solving Convex and Non-convex Functionals in Image Processing Using a Primal-dual Algorithm*. PhD thesis, Universität Regensburg.
- Bhaduri, A. (2021). Learning to live with covid? India may be entering endemic stage, says top doc. *Hindustan Times*.
- Björkegren, D. and Karaca, B. C. (2022). Network adoption subsidies: A digital evaluation of a rural mobile phone program in Rwanda. *Journal of Development Economics*, 154:102762.
- Blumenstock, J., Cadamuro, G., and On, R. (2015). Predicting poverty and wealth from mobile phone metadata. *Science*, 350(6264):1073–1076.
- Bosq, D. (2012). *Nonparametric statistics for stochastic processes: estimation and prediction*, volume 110. Springer Science & Business Media.
- Braun, J. V., Braun, R., and Müller, H.-G. (2000). Multiple changepoint fitting via quasi-likelihood, with application to dna sequence segmentation. *Biometrika*, 87(2):301–314.
- Brown, E. S., Chan, T. F., and Bresson, X. (2012). Completely convex formulation of the Chan-Vese image segmentation model. *International Journal of Computer Vision*, 98(1):103–121.
- Brunner, E. J., Dougherty, S. M., and Ross, S. L. (2021). The effects of career and technical education: Evidence from the connecticut technical high school system. *Review of Economics and Statistics*, pages 1–46.
- Caetano, G. and Maheshri, V. (2017). School segregation and the identification of tipping behavior. *Journal of Public Economics*, 148:115–135.
- Camilli, F. (1999). A note on convergence of level sets. *Zeitschrift für Analysis und ihre Anwendungen*, 18(1):3–12.

- Canny, J. (1986). A computational approach to edge detection. *IEEE Transactions on pattern analysis and machine intelligence*, (6):679–698.
- Card, D., Mas, A., and Rothstein, J. (2008). Tipping and the dynamics of segregation. *The Quarterly Journal of Economics*, 123(1):177–218.
- Caroccia, M., Chambolle, A., and Slepčev, D. (2020). Mumford–Shah functionals on graphs and their asymptotics. *Nonlinearity*, 33(8):3846.
- Cattaneo, M. D. and Titiunik, R. (2022). Regression discontinuity designs. *Annual Review of Economics*, 14:821–851.
- Chambolle, A. and Pock, T. (2011). A first-order primal-dual algorithm for convex problems with applications to imaging. *Journal of Mathematical Imaging and Vision*, 40(1):120–145.
- Chambolle, A. and Pock, T. (2021). Learning consistent discretizations of the total variation. *SIAM Journal on Imaging Sciences*, 14(2):778–813.
- Chambolle, A., Tan, P., and Vaiter, S. (2017). Accelerated alternating descent methods for dykstra-like problems. *Journal of Mathematical Imaging and Vision*, 59:481–497.
- Chan, T. F. and Shen, J. (2005). *Image processing and analysis: variational, PDE, wavelet, and stochastic methods*. SIAM.
- Chan, T. F. and Vese, L. A. (2001). Active contours without edges. *IEEE Transactions on Image Processing*, 10(2):266–277.
- Chen, H., Li, D., and Bar-Joseph, Z. (2023). Scs: cell segmentation for high-resolution spatial transcriptomics. *Nature methods*, 20(8):1237–1243.
- Cheng, A. (2023). Regression discontinuity designs with multiple running variables. *MIT working paper*.
- CISA (n.d.). Communications sector. <https://tinyurl.com/ycktyu7n>.
- Couture, V., Faber, B., Gu, Y., and Liu, L. (2021). Connecting the countryside via e-commerce: evidence from China. *American Economic Review: Insights*, 3(1):35–50.
- Dal Maso, G. (2012). *An introduction to Γ -convergence*, volume 8. Springer Science & Business Media.
- Delgado, M. A. and Hidalgo, J. (2000). Nonparametric inference on structural breaks. *Journal of Econometrics*, 96(1):113–144.
- Dong, L., Chen, S., Cheng, Y., Wu, Z., Li, C., and Wu, H. (2017). Measuring economic activity in China with mobile big data. *EPJ Data Science*, 6:1–17.
- Donoho, D. L. (1999). Wedgelets: Nearly minimax estimation of edges. *The Annals of Statistics*, 27(3):859–897.
- Donoho, D. L. and Johnstone, I. M. (1994). Ideal spatial adaptation by wavelet shrinkage. *Biometrika*, 81(3):425–455.
- Dubey, P. and Müller, H.-G. (2020). Fréchet change-point detection. *The Annals of Statistics*, 48(6):3312–3335.
- Eagle, N., Macy, M., and Claxton, R. (2010). Network diversity and economic development. *Science*, 328(5981):1029–1031.
- Evans, L. C. and Gariepy, R. F. (2018). *Measure theory and fine properties of functions*. Routledge.
- Federer, H. (2014). *Geometric measure theory*. Springer.
- Frias-Martinez, V. and Virseda, J. (2012). On the relationship between socio-economic factors and cell phone usage. In *Proceedings of the Fifth International Conference on Information and Communication Technologies and Development*, pages 76–84.

- Fryzlewicz, P. (2014). Wild binary segmentation for multiple change-point detection. *Annals of Statistics*.
- García Trillos, N. and Murray, R. (2017). A new analytical approach to consistency and overfitting in regularized empirical risk minimization. *European Journal of Applied Mathematics*, 28(6):886–921.
- García Trillos, N. and Slepčev, D. (2016). Continuum limit of total variation on point clouds. *Archive for Rational Mechanics and Analysis*, 220:193–241.
- Geman, S. and Geman, D. (1984). Stochastic relaxation, gibbs distributions, and the bayesian restoration of images. *IEEE Transactions on pattern analysis and machine intelligence*, (6):721–741.
- Goldfarb, A. and Tucker, C. (2019). Digital economics. *Journal of Economic Literature*, 57(1):3–43.
- Gunsilius, F. and Van Dijke, D. (2025). Free discontinuity regression: With an application to the economic effects of internet shutdowns. *arXiv preprint arXiv:2309.14630*.
- Hansen, B. E. (2017). Regression kink with an unknown threshold. *Journal of Business & Economic Statistics*, 35(2):228–240.
- Harchaoui, Z. and Lévy-Leduc, C. (2010). Multiple change-point estimation with a total variation penalty. *Journal of the American Statistical Association*, 105(492):1480–1493.
- Harchaoui, Z., Moulines, E., and Bach, F. (2008). Kernel change-point analysis. *Advances in Neural Information Processing Systems*, 21.
- Herlands, W., McFowland III, E., Wilson, A. G., and Neill, D. B. (2018). Automated local regression discontinuity design discovery. In *Proceedings of the 24th ACM SIGKDD International Conference on Knowledge Discovery & Data Mining*, pages 1512–1520.
- Herlands, W., Neill, D. B., Nickisch, H., and Wilson, A. G. (2019). Change surfaces for expressive multidimensional changepoints and counterfactual prediction. *J. Mach. Learn. Res.*, 20:99–1.
- Hjort, J. and Poulsen, J. (2019). The arrival of fast internet and employment in Africa. *American Economic Review*, 109(3):1032–1079.
- Horváth, L., Kokoszka, P., and Wang, S. (2021). Monitoring for a change point in a sequence of distributions. *The Annals of Statistics*, 49(4):2271–2291.
- Hou, W., Ji, Z., Chen, Z., Wherry, E. J., Hicks, S. C., and Ji, H. (2023). A statistical framework for differential pseudotime analysis with multiple single-cell rna-seq samples. *Nature communications*, 14(1):7286.
- Hu, A. J., Green, A., and Tibshirani, R. J. (2022). The voronoigram: Minimax estimation of bounded variation functions from scattered data. *arXiv preprint arXiv:2212.14514*.
- Human Rights Watch (2023). India: Internet shutdowns hurt vulnerable communities. Technical report, Human Rights Watch.
- Hütter, J.-C. and Rigollet, P. (2016). Optimal rates for total variation denoising. In *Conference on Learning Theory*, pages 1115–1146. PMLR.
- Irle, A. (1997). On consistency in nonparametric estimation under mixing conditions. *Journal of multivariate analysis*, 60(1):123–147.
- Jensen, R. (2007). The digital provide: Information (technology), market performance, and welfare in the south Indian fisheries sector. *The Quarterly Journal of Economics*, 122(3):879–924.
- Kass, M., Witkin, A., and Terzopoulos, D. (1988). Snakes: Active contour models. *Internation-*

- tional journal of computer vision*, 1(4):321–331.
- Kathuria, R., Kedia, M., Varma, G., Bagchi, K., and Sekhani, R. (2018). The anatomy of an internet blackout: measuring the economic impact of internet shutdowns in india. Technical report, Indian Council for Research on International Economic Relations.
- Keele, L. J. and Titiunik, R. (2015). Geographic boundaries as regression discontinuities. *Political Analysis*, 23(1):127–155.
- Killick, R., Fearnhead, P., and Eckley, I. A. (2012). Optimal detection of changepoints with a linear computational cost. *Journal of the American Statistical Association*, 107(500):1590–1598.
- Korostelev, A. P. and Tsybakov, A. B. (1993). *Minimax linewise algorithm for image reconstruction*. Springer.
- Kovács, S., Bühlmann, P., Li, H., and Munk, A. (2023). Seeded binary segmentation: a general methodology for fast and optimal changepoint detection. *Biometrika*, 110(1):249–256.
- Kreindler, G. E. and Miyauchi, Y. (2021). Measuring commuting and economic activity inside cities with cell phone records. *Review of Economics and Statistics*, pages 1–48.
- Kung, K. S., Greco, K., Sobolevsky, S., and Ratti, C. (2014). Exploring universal patterns in human home-work commuting from mobile phone data. *PLOS One*, 9(6):e96180.
- Kuo, R., Ho, L., and Hu, C. M. (2002). Integration of self-organizing feature map and k-means algorithm for market segmentation. *Computers & Operations Research*, 29(11):1475–1493.
- Lamberson, P. and Page, S. E. (2012). Tipping points. *Quarterly Journal of Political Science*, 7(2):175–208.
- Lei, J., G’Sell, M., Rinaldo, A., Tibshirani, R. J., and Wasserman, L. (2018). Distribution-free predictive inference for regression. *Journal of the American Statistical Association*, 113(523):1094–1111.
- Li, L., Chu, W., Langford, J., and Schapire, R. E. (2010). A contextual-bandit approach to personalized news article recommendation. In *Proceedings of the 19th international conference on World wide web*, pages 661–670.
- Li, M. and Ghosal, S. (2017). Bayesian detection of image boundaries. *The Annals of Statistics*, 45(5):2190–2217.
- Lucas, C.-G., Pascal, B., Pustelnik, N., and Abry, P. (2022). Hyperparameter selection for discrete Mumford–Shah. *Signal, Image and Video Processing*, pages 1–8.
- Madrid Padilla, C. M., Wang, D., Zhao, Z., and Yu, Y. (2022). Change-point detection for sparse and dense functional data in general dimensions. *Advances in Neural Information Processing Systems*, 35:37121–37133.
- Madrid Padilla, C. M., Xu, H., Wang, D., MADRID PADILLA, O. H., and Yu, Y. (2023). Change point detection and inference in multivariate non-parametric models under mixing conditions. *Advances in Neural Information Processing Systems*, 36:21081–21134.
- Mashal, M. and Kumar, H. (2023). Where digital payments, even for a 10-cent chai, are colossal in scale. *The New York Times*.
- Matteson, D. S. and James, N. A. (2014). A nonparametric approach for multiple change point analysis of multivariate data. *Journal of the American Statistical Association*, 109(505):334–345.
- Mattila, P. (1999). *Geometry of sets and measures in Euclidean spaces: fractals and rectifi-*

- ability. Number 44. Cambridge University Press.
- McKelvey, J. (1984). Simple transcendental expressions for the roots of cubic equations. *American Journal of Physics*, 52(3):269–270.
- Mishra, A. (2021). The internet cannot be suspended in entire districts to prevent cheating in exams - IFF writes to the Rajasthan government. *Internet Freedom Foundation*.
- Mollenhoff, T. and Cremers, D. (2017). Sublabel-accurate discretization of nonconvex free-discontinuity problems. In *Proceedings of the IEEE International Conference on Computer Vision*, pages 1183–1191.
- Morini, M. (2002). Global calibrations for the non-homogeneous Mumford–Shah functional. *Annali della Scuola Normale Superiore di Pisa-Classe di Scienze*, 1(3):603–648.
- Müller, H.-G. (1992). Change-points in nonparametric regression analysis. *The Annals of Statistics*, pages 737–761.
- Muller, H.-G. and Song, K.-S. (1994). Maximin estimation of multidimensional boundaries. *Journal of Multivariate Analysis*, 50(2):265–281.
- Mumford, D. B. and Shah, J. (1989). Optimal approximations by piecewise smooth functions and associated variational problems. *Communications on Pure and Applied Mathematics*.
- Naef, E., Muelbert, P., Raza, S., Frederick, R., Kendall, J., and Gupta, N. (2014). Using mobile data for development. Technical report, Cartesian and the Bill & Melinda Gates Foundation.
- Narita, Y. and Yata, K. (2021). Algorithm is experiment: Machine learning, market design, and policy eligibility rules. *arXiv:2104.12909*.
- O’Sullivan, F. and Qian, M. (1994). A regularized contrast statistic for object boundary estimation-implementation and statistical evaluation. *IEEE Transactions on Pattern Analysis and Machine Intelligence*, 16(6):561–570.
- Page, E. S. (1954). Continuous inspection schemes. *Biometrika*, 41(1/2):100–115.
- Park, C. (2022). Jump gaussian process model for estimating piecewise continuous regression functions. *The Journal of Machine Learning Research*, 23(1):12737–12773.
- Pock, T., Cremers, D., Bischof, H., and Chambolle, A. (2009). An algorithm for minimizing the Mumford–Shah functional. In *2009 IEEE 12th International Conference on Computer Vision*, pages 1133–1140. IEEE.
- Pock, T., Cremers, D., Bischof, H., and Chambolle, A. (2010). Global solutions of variational models with convex regularization. *SIAM Journal on Imaging Sciences*, 3(4):1122–1145.
- Politis, D. N., Romano, J. P., and Wolf, M. (1999). *Subsampling*. Springer Science & Business Media.
- Porter, J. and Yu, P. (2015). Regression discontinuity designs with unknown discontinuity points: Testing and estimation. *Journal of Econometrics*, 189(1):132–147.
- Purohit, D. (2022). 237 arrested in 4 years, yet exam mafia on a high in Rajasthan. *The Times of India*.
- Qiu, P. (1998). Discontinuous regression surfaces fitting. *The Annals of Statistics*, 26(6):2218–2245.
- Qiu, P. and Yandell, B. (1997). Jump detection in regression surfaces. *Journal of Computational and Graphical Statistics*, 6(3):332–354.
- Quelch, J. (2009). Quantifying the economic impact of the internet. Technical report, Harvard Business School.
- Ramani, S., Blu, T., and Unser, M. (2008). Monte-Carlo SURE: A black-box optimization of

- regularization parameters for general denoising algorithms. *IEEE Transactions on Image Processing*, 17(9):1540–1554.
- Richardson, T. J. (1992). Limit theorems for a variational problem arising in computer vision. *Annali della Scuola Normale Superiore di Pisa-Classe di Scienze*, 19(1):1–49.
- Rinaldo, A. (2009). Properties and refinements of the fused lasso. *The Annals of Statistics*, 37(5B):2922–2952.
- Röller, L.-H. and Waverman, L. (2001). Telecommunications infrastructure and economic development: A simultaneous approach. *American Economic Review*, 91(4):909–923.
- Rosson, Z., Anthonio, F., and Tackett, C. (2023). Weapons of control, shields of impunity: Internet shutdowns in 2022. *Access Now*.
- Ruf, M. (2019). Discrete stochastic approximations of the Mumford–Shah functional. In *Annales de l’Institut Henri Poincaré C, Analyse non linéaire*, volume 36–4, pages 887–937. Elsevier.
- Šćepanović, S., Mishkovski, I., Hui, P., Nurminen, J. K., and Ylä-Jääski, A. (2015). Mobile phone call data as a regional socio-economic proxy indicator. *PLOS One*, 10(4):e0124160.
- Scheffer, M., Bascompte, J., Brock, W. A., Brovkin, V., Carpenter, S. R., Dakos, V., Held, H., Van Nes, E. H., Rietkerk, M., and Sugihara, G. (2009). Early-warning signals for critical transitions. *Nature*, 461(7260):53–59.
- Software Freedom Law Center (2024). Internet shutdowns in india. <https://internetshutdowns.in/>.
- Spelta, A. and Pagnottoni, P. (2021). Mobility-based real-time economic monitoring amid the COVID-19 pandemic. *Scientific Reports*, 11(1):13069.
- Statcounter (2023). Mobile operating system market share India. <https://gs.statcounter.com/os-market-share/mobile/india>.
- Stein, C. M. (1981). Estimation of the mean of a multivariate normal distribution. *The Annals of Statistics*, pages 1135–1151.
- Stekalovskiy, E., Chambolle, A., and Cremers, D. (2012). A convex representation for the vectorial Mumford–Shah functional. In *2012 IEEE Conference on Computer Vision and Pattern Recognition*, pages 1712–1719. IEEE.
- Stekalovskiy, E. and Cremers, D. (2014). Real-time minimization of the piecewise smooth Mumford–Shah functional. In *European Conference on Computer Vision*, pages 127–141. Springer.
- Telecom Regulatory Authority of India (2023). The Indian telecom services performance indicators. <https://tinyurl.com/yj932ths>.
- The Economist (2021). Internet shutdowns have become a weapon of repressive regimes. <https://tinyurl.com/yc2jwbjz>.
- The Times of India (2023). Ban on mobile internet brings life in Jaipur to virtual standstill. <https://tinyurl.com/pa7263z9>.
- Tibshirani, R., Saunders, M., Rosset, S., Zhu, J., and Knight, K. (2005). Sparsity and smoothness via the fused lasso. *Journal of the Royal Statistical Society Series B: Statistical Methodology*, 67(1):91–108.
- Top10VPN (2023). The global cost of internet shutdowns. <https://www.top10vpn.com/research/cost-of-internet-shutdowns/>.
- United Nations High Commissioner for Human Rights (2022). Internet shutdowns: trends, causes, legal implications and impacts on a range of human rights. UN document, United

- Nations Human Rights Council. A/HRC/50/55.
- van der Vaart, A. W. and Wellner, J. A. (1996). *Weak convergence and empirical processes*. Springer.
- Van Dijcke, D., Wright, A. L., and Polyak, M. (2023). Public response to government alerts saves lives during Russian invasion of Ukraine. *Proceedings of the National Academy of Sciences*, 120(18):e2220160120.
- Wang, L.-L., Shi, Y., and Tai, X.-C. (2012). Robust edge detection using mumford-shah model and binary level set method. In *Scale Space and Variational Methods in Computer Vision: Third International Conference, SSVM 2011, Ein-Gedi, Israel, May 29–June 2, 2011, Revised Selected Papers 3*, pages 291–301. Springer.
- Wang, Y.-X., Sharpnack, J., Smola, A. J., and Tibshirani, R. J. (2016). Trend filtering on graphs. *Journal of Machine Learning Research*, 17(105):1–41.
- West, D. M. (2016). Internet shutdowns cost countries \$2.4 billion last year. *Center for Technological Innovation at Brookings, Washington, DC*.
- White, H. (2014). *Asymptotic theory for econometricians*. Academic press.
- Woloszko, N. (2020). Tracking activity in real time with Google Trends. Technical report, OECD.
- World Bank Group (2022). Ukraine, rapid damage and needs assessment August 2022. Technical report, World Bank Group.
- Yeung, J., Gupta, S., and Jha, M. (2021). Internet goes dark for millions in Indian state’s bid to stop exam cheats. *CNN Business*.
- Zhu, H., Fan, J., and Kong, L. (2014). Spatially varying coefficient model for neuroimaging data with jump discontinuities. *Journal of the American Statistical Association*, 109(507):1084–1098.
- Zuo, G. W. (2021). Wired and hired: Employment effects of subsidized broadband internet for low-income Americans. *American Economic Journal: Economic Policy*, 13(3):447–482.